Near-field atmospheric inversions for the localization and quantification of controlled methane releases using stationary and mobile measurements

Pramod Kumar, Grégoire Broquet, Christopher Caldow, Olivier Laurent, Susan Gichuki, Ford Cropley, Camille Yver-kwok, Bonaventure Fontanier, Thomas Lauvaux, Michel Ramonet, et al.

Received: 14 November 2021 | Revised: 21 February 2022 | Accepted: 30 March 2022

DOI: 10.1002/qj.4283

Quarterly Journal of the Royal Meteorological Society RMetS

RESEARCH ARTICLE

Near-field atmospheric inversions for the localization and quantification of controlled methane releases using stationary and mobile measurements

Pramod Kumar[1] | Grégoire Broquet[1] | Christopher Caldow[1] | Olivier Laurent[1] | Susan Gichuki[1] | Ford Cropley[1] | Camille Yver-Kwok[1] | Bonaventure Fontanier[1] | Thomas Lauvaux[1] | Michel Ramonet[1] | Adil Shah[1] | Guillaume Berthe[2] | Frédéric Martin[2] | Olivier Duclaux[3] | Catherine Juery[3] | Caroline Bouchet[4] | Joseph Pitt[5] | Philippe Ciais[1]

[1]Laboratoire des Sciences du Climat et de l'Environnement (LSCE/IPSL), CEA-CNRS-UVSQ, Université Paris-Saclay, Gif-sur-Yvette, France

[2]IFP Energies nouvelles-Géoscience, Rueil-Malmaison Cedex, France

[3]TotalEnergies Laboratoire Qualité de l'Air (LQA), Solaize Cedex, France

[4]SUEZ-Smart & Environmental Solutions, La Défense, France

[5]School of Marine and Atmospheric Sciences, Stony Brook University, Stony Brook, New York USA

Correspondence
P. Kumar, Laboratoire des Sciences du Climat et de l'Environnement (LSCE/IPSL), CEA-CNRS-UVSQ, Université Paris-Saclay, Gif-sur-Yvette, France.
Email: pramod.kumar@lsce.ipsl.fr

Present Address
Christopher Caldow, CSIRO, Land and Water, Canberra, GPO Box 1700, ACT 2601, Australia

Bonaventure Fontanier, Centrale Supélec, Université Paris-Saclay, Gif-sur-Yvette, 91192, France

Joseph Pitt, School of Chemistry, University of Bristol, Bristol, BS8 1TS, UK

Abstract

This study evaluates two local-scale atmospheric inversion approaches for the monitoring of methane (CH_4) emissions from industrial sites based on *in situ* atmospheric CH_4 mole fraction measurements from stationary or mobile sensors. We participated in a two-week campaign of CH_4 controlled-release experiments at TotalEnergies Anomaly Detection Initiatives (TADI) in Lacq, France in October 2019. We analyzed releases from various points within a 40 m × 50 m area with constant rates of 0.16 to 30 g CH_4 s^{-1} over 25 to 75 mins, using fixed-point and mobile measurements, and testing different inversion configurations with a Gaussian dispersion model. An inlet switching system, combining a limited number (6–7) of high-precision gas analyzers with a higher number (16) of sampling lines, ensured that a sufficient number of fixed measurement points sampled the plume downwind of the sources and the background mole fractions for any wind direction. The inversions using these fixed-point measurements provide release rate estimates with approximately 23%–30% average errors and estimates of the location of the releases with approximately 8–10 m average errors. The inversions using the mobile measurements provide estimates with approximately 20%–30% average errors for the release rates and approximately 30 m average errors for the release locations. The precision of the release rate estimates from both inversion frameworks corresponds to the best estimation

Funding information
ANR French national research agency, TotalEnergies-Raffinage Chimie, SUEZ, and THALES ALENIA SPACE, Grant/Award Number: ANR-17-CHIN-0004-01; French national research agency

precision documented on site-scale CH_4 inversions. However, the use of continuous measurements from fixed stations provides much more robust estimates of the source locations than that of the mobile measurements.

KEYWORDS
atmospheric inversion, controlled CH_4 release experiments, facility-scale methane emission, source term estimation, stationary and mobile measurements

1 | INTRODUCTION

The precise and efficient monitoring (hereafter referring to detection, localization and quantification) of fugitive methane (CH_4) industrial releases is essential to achieve cost-effective and quantifiable CH_4 anthropogenic emission mitigation. CH_4 is a significant greenhouse gas (GHG) linked to climate change impacts. Overall data show that global methane emissions have risen by about 15 to 20 Tg year^{-1} in the years from 2007 to 2014 (Nisbet *et al.*, 2014) and about 60% (range of 50%–70%) of global methane emissions come from anthropogenic activities (IPCC, 2013; Saunois *et al.*, 2020). Methane has a diverse range of natural and anthropogenic sources. The oil and natural-gas industry is one of the major sources of anthropogenic methane emissions (Zavala-Araiza *et al.*, 2015; Alvarez *et al.*, 2018; Saunois *et al.*, 2020). CH_4 emissions from upstream and downstream oil and natural-gas sectors are estimated to represent 63% of total fossil CH_4 emissions for the 2008–2017 decade (Saunois *et al.*, 2020).

Atmospheric techniques for the accurate monitoring of the CH_4 emissions primarily rely on appropriate measurements of the CH_4 mole fraction in the atmosphere. Fortunately, there have been marked developments in recent decades regarding measurement techniques, sensors, platforms and analytics. Sampling techniques used to monitor CH_4 emissions involve ground-based mobile laboratories, stationary sensors, aircraft, unmanned aerial vehicles (UAVs), and satellites (Fox *et al.*, 2019). Each of these techniques offers its own set of advantages and disadvantages. A suite of techniques is often required to achieve accurate monitoring of CH_4 emissions (Fox *et al.*, 2019 and others). For example, whilst satellites may offer broad spatial and temporal coverage, their detection limit using currently available measurement technology is assumed to be on the order of 100 g CH_4 s^{-1} or more, while a major part of industrial emissions consists of sources with much smaller rates (Frankenberg, 2005; Jacob *et al.*, 2016; Hu *et al.*, 2018; Varon *et al.*, 2018; Fox *et al.*, 2019; de Gouw *et al.*, 2020; Zhang *et al.*, 2020). On the other hand, stationary *in situ* sensors located close to or within an area with emitting sites offer a much lower detection limit. However, the deployment of networks of sensors that are sufficiently dense to ensure the continuous and exhaustive monitoring of the CH_4 emissions from a site is currently limited by cost. More specifically, it is limited by the lack of commercially available and reliable low-cost CH_4 sensors (e.g., Fox *et al.*, 2019; Mønster *et al.*, 2019 and references therein). Mobile ground laboratories can alleviate part of this issue as spatial coverage is provided by moving the measurement platform rather than having multiple sensors (e.g., Brantley *et al.*, 2014; Albertson *et al.*, 2016; Ars *et al.*, 2017; Zhang *et al.*, 2020; Kumar *et al.*, 2021). This allows for a low detection limit at relatively low cost and provides the ability to screen emissions from large or multiple facilities. The potential to localize sources can also be strongly enhanced by the use of mobile measurements following tracks converging towards such sources (Albertson *et al.*, 2016; von Fischer *et al.*, 2017). However, the main limitation of mobile ground laboratories is that they are generally labour-intensive and cannot be used continuously for a given site. Their use is generally restricted to specific measurement campaigns and therefore the sampling technique offers less temporal coverage than stationary sensors. Furthermore, mobile ground laboratories (typically within road vehicles) may have limited access to areas downwind of the sources depending on the meteorological conditions and on the road configuration. Hybrid approaches have been tested combining mobile monitoring to identify the location of the plume from the source and of the source itself with sequences of stationary measurements within this plume (Foster-Wittig *et al.*, 2015; Edie *et al.*, 2020; FprEN-17628, 2021).

In all cases, accurate quantification of methane emissions from facility-scale sources remains a challenge and large discrepancies may exist in estimates obtained from different measurement and modelling approaches (e.g., Alvarez *et al.*, 2018, Fox *et al.*, 2019, Mønster *et al.*, 2019). Atmospheric transport inverse modelling strategies relying on atmospheric dispersion modelling and on its simple or statistical inversion, are often used to tackle both the localization and quantification of sources (Ars *et al.*, 2017; Kumar *et al.*, 2021). Controlled-release experiments with known location and emission rates have

been conducted to support the development and evaluation of different measurement and modelling approaches and to improve the accuracy, reliability and applicability of anthropogenic methane emission monitoring at the facility-level scale (Loh *et al.*, 2009; Brantley *et al.*, 2014; Luhar *et al.*, 2014; Albertson *et al.*, 2016; Ars *et al.*, 2017; Feitz *et al.*, 2018; Ravikumar *et al.*, 2019; Edie *et al.*, 2020; Shah *et al.*, 2020; Kumar *et al.*, 2021). Such experiments reveal that the current level of uncertainties in the emission estimates hardly reach values lower than 30% (Brantley *et al.*, 2014; Foster-Wittig *et al.*, 2015; Albertson *et al.*, 2016; FprEN-17628, 2021; Kumar *et al.*, 2021). Similar approaches have been used and similar tests have been conducted to support the monitoring of site-scale emissions of pollutants for a long time. Even if facing different types of atmospheric background and even if based on different types of instruments with different levels of precision and with different constraints for deployment on sites, the most recent studies provide levels of relative uncertainty in the estimates of pollutant emissions that are similar to that for CH_4 (Ben Salem, 2014).

TotalEnergies developed a programme of controlled-release experiments at the TotalEnergies Anomaly Detection Initiatives (TADI) test site at Lacq in southwestern France to test different atmospheric measurement and modelling techniques to monitor GHG emissions in various release scenarios corresponding to the oil and gas extraction industries. We participated in two campaigns in a series of such controlled-release experiments at TADI within the framework of the TRAcking Carbon Emissions (TRACE) programme (https://trace.lsce.ipsl.fr/). Kumar *et al.* (2021) described the mobile near-surface CH_4 and CO_2 measurements (from a car) and inverse modelling method applied during the one-week campaign in October 2018 (TADI-2018) and the corresponding results. The campaign featured very brief (4–8 mins) CH_4 and CO_2 controlled releases from point sources with relatively poor wind conditions. The results indicated that we obtained approximately 10%–40% average error in the release rates. However, the study showed that the precise location of these brief releases within the emission area of approximately 40 m × 50 m was challenging, since we obtained approximately 30–40 m errors in the estimate of the locations of the releases.

This new study relates to the measurements, modelling and analysis conducted for the two-week campaign in October 2019 (TADI-2019), during which CH_4 was emitted at approximately 0.15 to 150 g CH_4 s^{-1} rates. Some controlled releases of CO_2 and mixtures of CH_4 with CO_2, C_2H_6 or C_3H_8 were also conducted during this campaign but we focussed our analysis on the CH_4 releases. These CH_4 controlled releases were dedicated to test the systems for the long-term monitoring of emissions mainly for environmental purposes. They were thus significantly longer (between 25 and 75 mins) than those during TADI-2018, which were primarily dedicated to the test of safety surveillance systems. This and more favourable meteorological conditions than during TADI-2018 (with stronger winds) gave us the opportunity to install and test the capabilities of a network of a limited (i.e., <20) number of stationary CH_4 (*in situ*) continuous measurement points. These measurements relied on 6–7 high-precision gas analyzers each connected to one of 16 possible sampling lines with inlets around the release areas. We conducted these stationary measurements in parallel to a similar mobile CH_4 measurement technique as that used during TADI-2018.

In addition to providing accurate estimates of the release location and rates, the specific objectives of our analysis of these data based on a Gaussian plume model (as in Kumar *et al.*, 2021) and presented here are to: (a) evaluate whether the length of the releases, larger in TADI-2019 than during TADI-2018, and the more favourable wind conditions allow for more precise estimates of the release rates and location when using the same mobile measurement and inversion method as in Kumar *et al.* (2021); (b) develop and apply an adapted inversion method to derive accurate estimates of the release rate and location based on the data from the few fixed measurement points that fell within the CH_4 plumes during individual releases; and (c) compare the precision of the estimates from the two coupled observation-inversion methods.

Regarding (a), the inversion technique used by Kumar *et al.* (2021) to estimate the single-point release location and rates from the near-surface mobile measurements, relied on the fit between the modelled and observed areas of individual methane mole fraction plume cross-sections and between the measured winds and the directions from the source location estimate to these individual plume cross-sections. Longer releases allow for increasing the number of plume cross-sections, which should thus increase the precision of such a method. Kumar *et al.* (2021) often had to rely on less than three plume cross-sections per release during TADI-2018, and they had expectations that the use of the releases longer than 30 min would allow them to catch more than 10 plume cross-sections (Caulton *et al.*, 2018) with the type of car measurements that can be conducted at the TADI. Furthermore, several diagnostics by Kumar *et al.* (2021) indicated that their results were strongly impacted by the model errors associated to the simulation of the plume cross-sections with a Gaussian plume model and by our limited skill to characterize it. Wind speeds larger than those encountered during TADI-2018 were expected to decrease this model error.

Regarding (b) and (c), inversion techniques relying on networks of fixed measurement points to localize and quantify sources of pollutants have been developed for a long time (Bocquet, 2005; Keats *et al.*, 2007; Sharan *et al.*, 2009; Luhar *et al.*, 2014; Feitz *et al.*, 2018). They usually rely on the comparison between modelled and observed long-term averages of the concentrations at measurement locations (Keats *et al.*, 2007; Sharan *et al.*, 2009; Luhar *et al.*, 2014; Feitz *et al.*, 2018). However, they usually exploit a number of measurement points (Keats *et al.*, 2007; Sharan *et al.*, 2009; Kumar *et al.*, 2015) and/or on durations (over several days for instance in Feitz *et al.*, 2018 and Luhar *et al.*, 2014) that exceed by far the number of measurements point and/or the duration of the releases we could have for TADI-2019. To our knowledge, there have been only a very limited number of experiments and studies of CH_4 emission estimation using such fixed-point measurements (Luhar *et al.*, 2014; Feitz *et al.*, 2018). Here, we propose a specific inversion technique, which, similar to Kumar *et al.* (2021), takes advantage of the variation of the wind to increase the constraint on the inversion of the locations and rates of single CH_4 release points. It thus compares modelled and observed averages of the concentrations at the measurement locations binned over relatively short periods of time or within sectors of wind directions (with two versions of this inversion technique being tested).

We present our fixed-point and mobile near-surface measurements, analysis, inversions, and the comparison of the results to actual release location and rates during the TADI-2019 campaign. We focus on the analysis of single CH_4 point-source releases only because we consider that our limited number of fixed measurement points is not sufficient to allow for a robust separation of overlapping plumes from multiple CH_4 sources. Section 2 describes the experimental setup for the fixed-points, near-surface mobile and meteorological measurements. The inversion methods for each type of measurement are presented in Section 3. Section 4 presents the results and their comparison to actual release location and rates, followed by a discussion in Section 5 and a conclusion in Section 6.

2 | TADI-2019 CAMPAIGN

The TADI-2019 campaign was conducted during October 2–10, 2019 at TotalEnergies's controlled-release test site TADI located in Lacq, northwest of Pau in southwestern France (latitude: 43.413°N, longitude: 0.642°W). The TADI site is an area of approximately 200 m × 200 m containing a variety of decommissioned oil and gas equipment such as pipes, valves, tanks, columns, well heads and flares, which are typically found at operational natural-gas extraction facilities. Leak points were created at different locations and heights in these pieces of equipment to mimic realistic leak sources in industrial facilities. The terrain of the TADI platform is predominantly flat and homogeneous but there are some obstacles to atmospheric dispersion such as tanks located on the platform as well as shipping containers and tents located in the areas adjacent to the platform. Further details about the features of the platform and surrounding areas that may influence the wind and gas dispersion can be found in Kumar *et al.* (2021). The location of the controlled releases during the campaign was restricted to a 40 m × 50 m ATmosphere EXplosive (ATEX) zone. Figure 1 shows a schematic of the TADI platform including the ATEX zone and the experimental setup for the meteorological, fixed-point and mobile measurements. The orientation of TADI platform is 26.4° east of true north (Figure 1).

During the TADI-2019 campaign, a total of 40 controlled releases covering a large range of magnitudes were carried out: 32 releases with single CH_4 sources of 0.16 to 150 g CH_4 s^{-1} (on which the analyses here are focussed), six releases including multiple and simultaneous CH_4 sources (sometimes combined with CO_2, C_2H_6, and C_3H_8 sources), and two releases with CO_2 sources. Each release lasted between 25 and 75 mins and gas was released at heights ranging from 0.39 to 6 m above the ground. For each CH_4 controlled release from a single source, we measured the mole fraction of CH_4 in the atmosphere at fixed points and from a car as well as meteorology and atmospheric turbulence. The details of these measurements and the experimental setup are presented in following subsections.

2.1 | Atmospheric CH_4 measurements

2.1.1 | Fixed-point measurements

Our measurements correspond to near-field dispersion over the TADI platform, where the atmospheric travel time from an emitting point source to the measuring tripod locations is generally much shorter than the duration of the releases. We installed 16 tripods at fixed points, nearly equally spaced on a circle around the ATEX zone (i.e., the release area, Figure 1). The practical constraints limited the number of measurement locations to 16 and the number of simultaneously active measurement points to 6–7 at any one time since we relied on seven high-precision gas analyzers based on spectroscopy technology. Therefore, our strategy was to deploy such a circle of measurement points to ensure several points of plume intersection, regardless of wind direction, which was known to be potentially highly variable in the area (Kumar *et al.*, 2021).

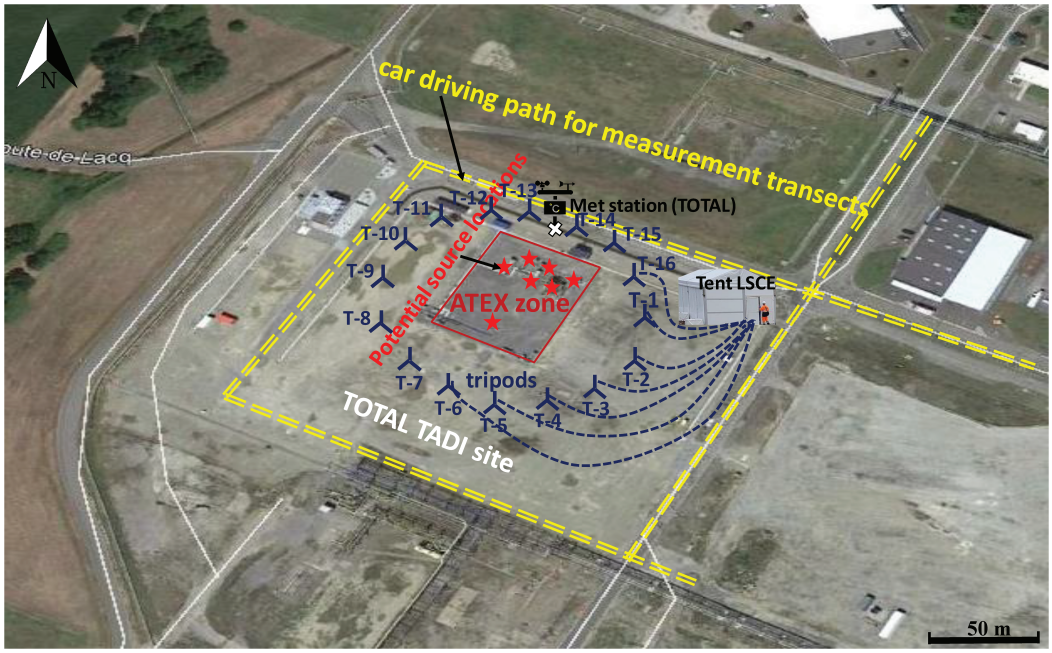

FIGURE 1 A schematic diagram of the experimental setup on a satellite image of the TotalEnergies Anomaly Detection Initiatives (TADI) platform (source: Google earth©). The red stars show examples of the possible location of the releases in the ATEX zone (rectangle with solid red coloured line) during the TADI-2019 campaign (see the full set of exact locations in Figure S1 in the Supplementary information material). The dark blue symbols labelled T-1 to T-16 indicate the location of the 16 tripods where the inlets for fixed-point measurements were located, while the dark blue dashed lines are indicative of the 16 sampling lines that run separately from each tripod to the tent where the seven gas analyzers were located (white structure). The yellow-coloured double dotted lines show the main driving paths for the ground-based mobile measurement platform. The meteorological station installed by TotalEnergies was located at the basis of the black symbols [Colour figure can be viewed at wileyonlinelibrary.com]

The switching of different sampling lines between active and passive was performed manually depending on the atmospheric dispersion (on the wind direction and its variability). The aim was to optimize the number of active air inlets that sampled within the gas plume downwind of the source during each release, whilst still obtaining a clear measurement of the 'background', that is, of the CH_4 atmospheric mole fractions baseline field corresponding to the large-scale mole fraction and to external emissions, excluding the signature of the plume from the source.

Each of the 16 tripods was equipped with a dedicated air intake at a height of 2.75–3.50 m and connected to a 6.35 mm diameter Synflex® 1,300 sampling line that ran on the ground to a tent about 10–100 m from the ATEX zone where most of the equipment was installed. The active sampling lines were continuously flushed at a rate of approximately 6 L min^{-1} with a dedicated in-line flushing pump (KNF N811 with PTFE diaphragm). Downstream of the pump, the air was split three ways to: (a) a high-precision gas analyzer; (b) a low-cost semiconductor-based CH_4 sensor currently under development (whose results are not presented here; Rivera *et al.* in prep.); and (c) a vent to maintain the line close to atmospheric pressure. The high-precision gas analyzers consisted of four Picarro G2401 cavity ring-down spectrometers(CRDS) analyzers that measure CH_4, CO_2, CO and H_2O, two Picarro G2201-*i* isotopic CRDS analyzers for $^{13}CH_4$, $^{12}CH_4$, $^{13}CO_2$, $^{12}CO_2$ and H_2O, and one ABB Micro-portable Greenhouse Gas Analyzer (MGGA) measuring CO_2, CH_4 and H_2O. Each gas analyzer measured the H_2O mole fraction to correct the water vapour effect and provide the mole fraction in dry air. Continuous mole fraction measurements from each analyzer were made at approximately 0.3–1 Hz. Before and at the end of the campaign, two calibration sequences were performed for all the analyzers. They showed a good linearity over a wide range of CH_4 and CO_2 mole fractions (see Kumar *et al.*, 2021 for details).

For each active combination of sampling line and gas analyzer, we determined a time delay which accounts for: (a) the time taken for air to travel from the inlet to the gas analyzer; (b) the response time of the gas analyzer; and (c) the offset between the clock on the gas analyzer and UTC time. To achieve this, we spiked the inlet with a short exhalation of breath at a specific UTC time provided by a Global Positioning Satellite (GPS) module, and measured the time taken to detect a CO_2/H_2O response on the corresponding gas analyzer. This time delay was subtracted from the raw

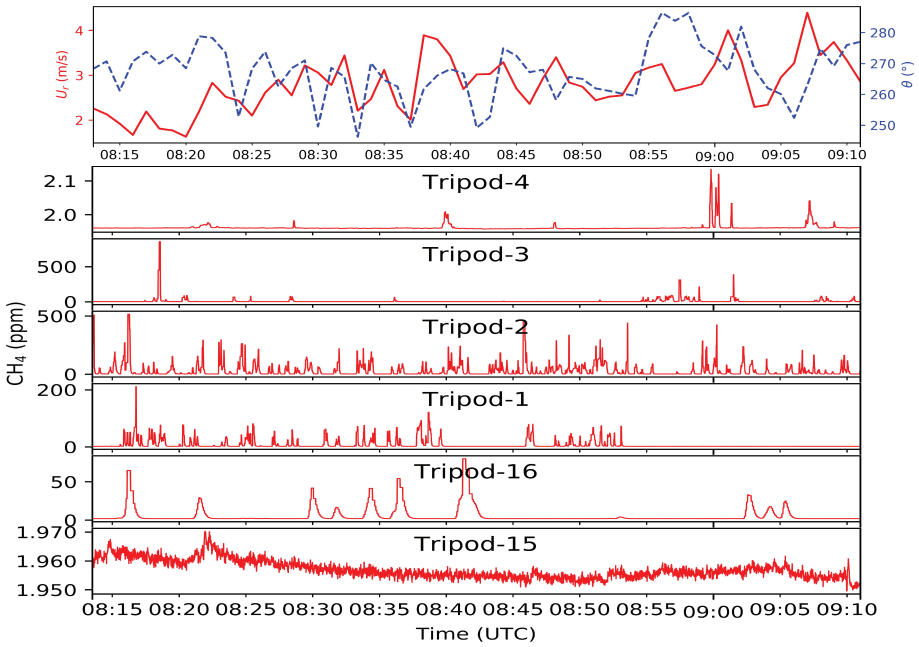

FIGURE 2 Time series of 1-min averaged wind speed (U_r) (solid line on left y-axis) and direction (θ) (dotted line on right y-axis) from TOTALEnergies' 3D sonic anemometer and CH4 mole fraction measured by the analyzers connected to the active tripods at different locations at the TADI site for release-1 (emission rate: 10 g CH_4 s^{-1}) on 2 October 2019 [Colour figure can be viewed at wileyonlinelibrary.com]

time stamp in order to synchronize all observations from the gas analyzers to UTC time provided by a GPS module, to which other instrumentation such as the meteorological station was also synchronized.

An overview of the time-series of the instantaneous CH_4 mole fraction measured at six active and adjacent tripods in and around the CH_4 plume during the first controlled release (release-1) is shown in Figure 2. This figure also shows variations in wind speed (U_r) and direction (θ) which were quite steady during this release. It implicitly provides the evolution in time over approximately 1 hr of discrete sampling of a section across the plume whose shape and position vary depending on the wind speed and direction and the associated turbulence. During this release, the wind was mostly blowing from the west, and the source was located in the southeast quadrant of the ATEX zone. Tripods T-4 and T-15 mostly sampled background air while the centre of the plume section seemed to oscillate between T-1 and T-3. T-2 and T-3 measured CH_4 mole fractions reaching or exceeding 500 ppm (Figure 2).

2.1.2 | Mobile measurements

Near-surface mobile concentration measurements were made with a Picarro G2210-*i* analyzer which simultaneously measures $\delta^{13}CH_4$ and C_2H_6-to-CH_4 ratio as well as CO_2 and H_2O vapour. The gas analyzer was installed in a vehicle (hybrid electric Mitsubishi SUV) which was driven along the roads adjacent to the TADI site to conduct the mobile measurements downwind of the releases, targeting plume cross-sections (Figure 1; and see also Kumar *et al.*, 2021). In addition, GPS time and position were measured from the vehicle. During all experiments, the sampling inlet of the analyzer was approximately 2 m above the ground. Time delays and clock synchronization were empirically corrected by spiking the inlet in the same manner as for the fixed-point measurements (see Section 2.1.1). Figure 3 shows an example of an observed CH_4 mole fraction time-series and plume cross-sections from the mobile measurements along the roads adjacent to the TADI platform during release-1. As illustrated in Figure 3, approximately 15 plume cross-sections were obtained during this release.

2.1.3 | Background mole fractions

The background mole fractions during individual CH_4 releases were simply calculated as the minimum value of the corresponding mole fraction time-series from fixed-point and mobile measurements (Kumar *et al.*, 2021). These CH_4 background values are subtracted from the measurement time-series to derive the enhancement corresponding to the plumes from the controlled releases.

2.2 | Meteorological and turbulence data

Reliable meteorological and turbulence data are essential to determine the near-surface wind flow and the state of the atmospheric boundary layer during a gas release, and thus to support the definition of suitable

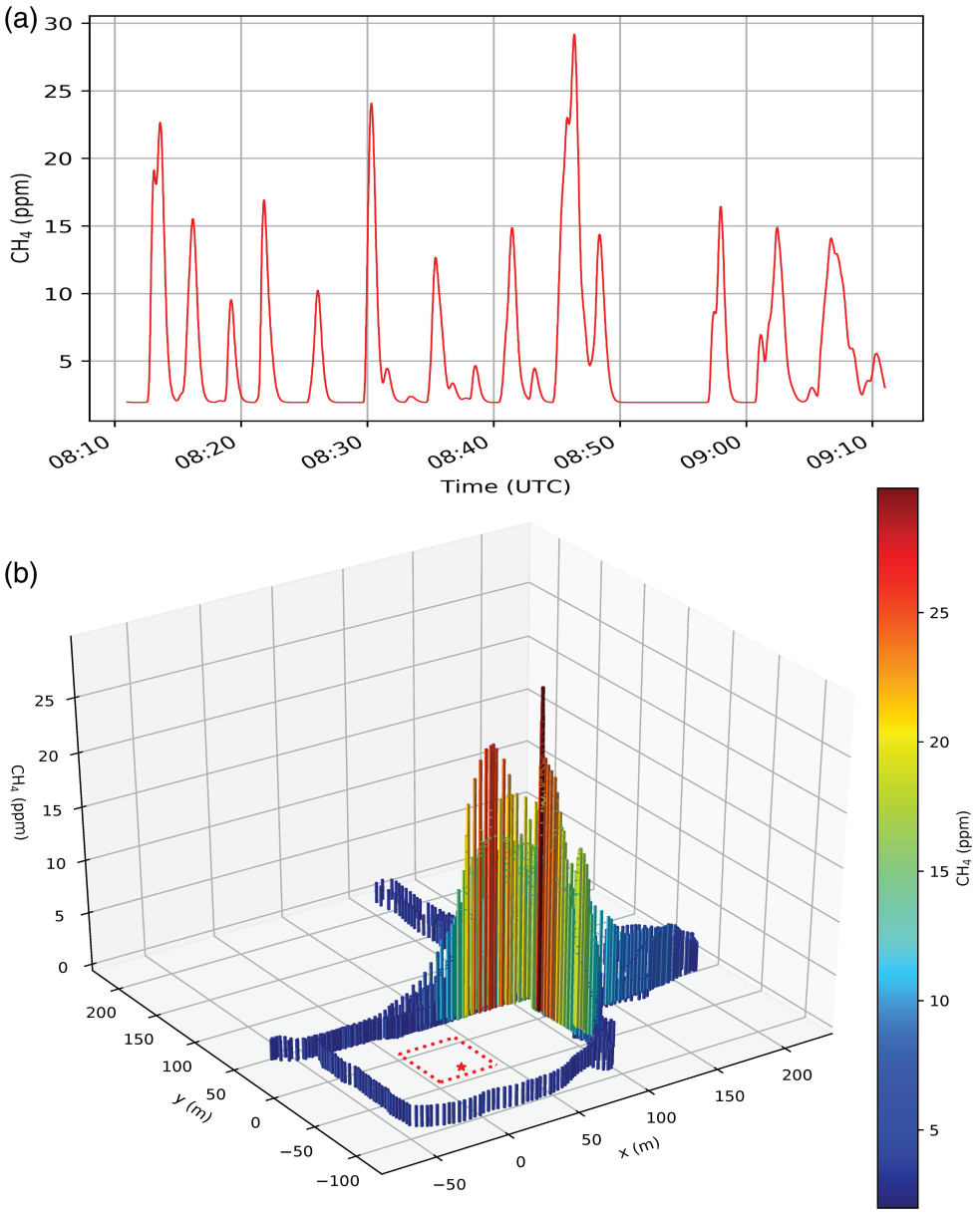

FIGURE 3 (a) Time series and (b) 3D representation of CH_4 mole fractions from mobile measurements during release-1. The red star shows the source location in the ATmosphere EXplosive (ATEX) zone during this release [Colour figure can be viewed at wileyonlinelibrary.com]

parameters for the atmospheric dispersion model. A meteorological station was installed by TotalEnergies on the TADI platform (Figure 1). The TotalEnergies meteorological station included a Metek Sonic three-dimensional (3D) anemometer installed at a reference height (z_r) of 5 m above the ground surface. It collected 1-min averaged meteorological and turbulence data of wind speed (U_r), wind direction (θ), sonic temperature (T), the Monin–Obukhov stability parameter ($1/L$) (where L is the Obukhov length), surface friction velocity (u_*), and standard deviation of wind velocity fluctuations in all three dimensions (σ_u, σ_v, σ_w). The standard deviation of wind direction (σ_θ) over a release period is calculated from 1-min wind direction averages. These meteorological and turbulence data are averaged over windows ranging from several minutes to full release periods (depending on whether we process mobile measurements or fixed measurements, and when processing the latter, depending on their temporal binning) to parameterize the wind flow and diffusion parameters in our plume dispersion model described in Section 3.1. Hereafter, the notations U_r, θ, T, L, u_*, σ_θ, and (σ_u, σ_v, σ_w) represent such averages over the corresponding temporal windows rather than the 1-min data.

2.3 | Meteorological conditions and selection of the controlled releases for the inversions

During six of the 32 single CH_4 source releases, wind speed averages over the release periods were below 0.6 m s^{-1}.

Such low wind speed conditions are not suitable for use within a Gaussian plume model in our inverse modelling framework (Thomson and Manning, 2001; Kumar *et al.*, 2021). We thus excluded these six releases from our inversion tests. Therefore, we conducted inversions for 26 CH_4 releases. However, seven out of these 26 releases still correspond to wind speeds whose average over the duration of a given release, U_r, is less than approximately 1.5 m s^{-1}, called hereafter 'low wind speed conditions'. For all 26 releases, fixed-point CH_4 measurements were used but, for practical reasons, we could not conduct mobile measurements for one of these releases (release-9).

Table 1 summarizes information on the release location and rate and on the meteorological and turbulence parameters for the 26 releases for which we conducted inversions. It also presents the number of cross-sections (denoted 'peaks' in this table) made during the mobile measurements for each release. All releases and measurements were conducted during day time. The sign and magnitude of the Monin–Obukhov stability parameter ($1/L$) computed over each release period indicate that the atmospheric stability varied from near-neutral to convective stability conditions ($L<0$) during these releases.

TABLE 1 Summary of the data for the selected CH_4 releases and corresponding mean velocity and turbulence statistics over the release periods measured with TotalEnergies 3D sonic anemometer at a height of 5 m above the ground

Release no.	Duration (D_s; h:mm)	No. of peaks	q_s (g s^{-1})	z_s (m)	U_r (m s^{-1})	θ (°)	σ_θ (°)	L (m)	u_* (m s^{-1})	σ_u (m s^{-1})	σ_v (m s^{-1})	σ_w (m s^{-1})
1	0:58	11	10	0.96	2.76	267	9	−58	0.22	0.52	0.51	0.39
2	1:00	19	30	0.75	3.76	289	10	−140	0.35	0.74	0.73	0.56
3	0:32	11	1	0.39	3.31	308	18	−137	0.38	0.76	0.80	0.55
4	0:33	9	0.5	1.90	3.56	304	9	−121	0.39	0.73	0.73	0.54
5	0:33	8	5	2.50	3.91	277	12	−47	0.31	0.66	0.65	0.54
6	0:35	5	3	3.0	0.65	108	41	−10	0.12	0.19	0.20	0.22
7	0:38	6	1	0.61	1.46	319	43	−34	0.21	0.43	0.38	0.33
8	0:38	5	0.5	0.59	2.17	277	34	−25	0.24	0.46	0.46	0.37
9	0:30	N/A	0.16	0.61	2.39	286	21	−27	0.23	0.55	0.49	0.37
10	0:46	12	1	6.0	0.93	144	31	−40	0.09	0.15	0.15	0.15
11	1:01	20	2	2.22	3.50	294	9	−194	0.37	0.69	0.69	0.53
12	0:44	15	2	1.90	1.83	138	11	−26	0.14	0.26	0.26	0.22
13	0:50	14	4	2.44	1.45	145	14	−16	0.12	0.21	0.19	0.19
14	0:44	11	1	1.90	1.31	257	42	−15	0.19	0.36	0.35	0.32
15	0:33	18	1	1.90	1.11	233	49	−28	0.18	0.36	0.35	0.29
16	0:50	9	2	1.90	1.84	141	9	−28	0.15	0.26	0.23	0.24
17	0:35	16	5	1.84	3.12	291	13	−69	0.30	0.62	0.61	0.47
18	0:48	6	0.4	0.39	2.73	301	20	−45	0.31	0.57	0.62	0.44
19	0:37	17	0.5	1.26	3.12	297	17	−53	0.30	0.63	0.61	0.46
20	0:44	11	0.6	0.59	1.07	208	27	−40	0.14	0.24	0.27	0.21
21	0:44	12	1	2.22	1.51	238	19	−77	0.16	0.31	0.32	0.25
22	0:24	10	2	6.0	1.70	238	9	−50	0.18	0.36	0.34	0.29
23	0:34	13	4	0.39	3.58	283	17	−206	0.33	0.67	0.69	0.51
24	0:45	16	2	1.29	2.49	282	21	−167	0.27	0.60	0.56	0.43
25	0:59	13	2	0.59	1.28	139	20	−12	0.13	0.22	0.21	0.22
26	0:36	6	0.5	0.61	0.73	116	36	−35	0.15	0.26	0.22	0.25

Note: Here, q_s and z_s are the actual release rate and height of source, respectively. Grey shades correspond to the releases for which U_r <1.5 m s^{-1}.

3 | ATMOSPHERIC INVERSION OF THE RELEASE LOCATION AND RATES

3.1 | Dispersion model and adjoint source–receptor relationship

3.1.1 | The Gaussian plume dispersion model

The atmospheric transport of CH_4 has regularly been modelled as that of a passive tracer at the local scales to mesoscales, and in particular, for short-range dispersion simulations, using Gaussian plume models (Foster-Wittig *et al.*, 2015; Albertson *et al.*, 2016; Riddick *et al.*, 2017; Bergamaschi *et al.*, 2018; Feitz *et al.*, 2018; Pison *et al.*, 2018; Zhou *et al.*, 2019). Here, both the inversions using the mobile measurements and those using the fixed measurement points rely on the Gaussian plume model presented in Kumar *et al.* (2021). Several parameters have been updated in this study compared to the configuration presented in Kumar *et al.* (2021), mainly the enhancement of the spread of the plume for low wind speed conditions and the use of a power-law wind profile to define the effective mean wind speed U_{eff} at the release height.

Depending on the inversion framework, the Gaussian plume model is driven by an effective mean wind direction given by the meteorological or CH_4 mole fractions data, and by the effective wind speed U_{eff} given by the meteorological data in all cases. Considering a Cartesian coordinate system where the X and Y axis are defined by the effective mean wind direction, this model formulates the gas concentration $C(X, Y, Z)$ at the coordinates (X, Y, Z) (for positive X and Z), corresponding to the plume from a point source whose effective release is located at $(0, 0, z_{\text{eff}})$ with release rate q as

$$C(X,Y,Z) = \frac{q}{2\pi\sigma_Y\sigma_Z U_{\text{eff}}} \exp\left(\frac{-Y^2}{2\sigma_Y^2}\right) \times \left[\exp\left(\frac{-(Z-z_{\text{eff}})^2}{2\sigma_Z^2}\right) + \exp\left(\frac{-(Z+z_{\text{eff}})^2}{2\sigma_Z^2}\right)\right] \quad (1)$$

where z_{eff} is the effective release height above the ground surface (see Section 3.2), U_{eff} is the effective mean wind speed at z_{eff} (which is the effective height of the plume centerline) and the standard deviations σ_Y and σ_Z of the concentration distribution in lateral (Y) and vertical (Z) directions, respectively (known as dispersion coefficients) are parameterized as (Gryning *et al.*, 1987)

$$\sigma_Y = \sigma_v t\left(1 + \sqrt{\frac{t}{2T_Y}}\right)^{-1} \quad (2a)$$

$$\sigma_Z = \sigma_w t\left(1 + \sqrt{\frac{t}{2T_Z}}\right)^{-1} \quad (2b)$$

where σ_v and σ_w are the standard deviation of the turbulent velocity fluctuations in lateral and vertical directions, respectively, T_Y and T_Z are the Lagrangian time scales, and t $(=X/U_{\text{eff}})$ is the travel time from origin to X. We take $T_Y = 200\,\text{s}$ (Draxler, 1976) for near-surface release and $T_Z = 300\,\text{s}$ for unstable conditions ($L<0$) (Gryning *et al.*, 1987). Under low wind conditions ($U_{\text{eff}} < 1.5\,\text{m s}^{-1}$) the wind direction becomes more variable. In order to account for this, when $U_{\text{eff}} < 1.5\,\text{m s}^{-1}$, the lateral spread of the plume is enhanced by following

$$\sigma_Y = \sqrt{\left(\sigma_v t\left(1 + \sqrt{\frac{t}{2T_Y}}\right)^{-1}\right)^2 + (\sigma_v t)^2} \quad (2c)$$

instead of Equation (2a) to parameterize it. A similar parameterization of σ_Y has been used in some advanced Gaussian plume dispersion models like ADMS5.2 where the first and second terms in Equation (2c) respectively correspond to the atmospheric turbulence and to large-scale variations in the direction of the wind (Carruthers *et al.*, 2020). The meteorological and turbulent dispersion parameters in the dispersion model are driven by the measurements from the TotalEnergies' 3D sonic anemometer data at 5 m height above the ground surface.

In order to characterize the variation of mean wind speed in the vertical direction, the mean wind speed at a vertical height (Z) in the atmospheric surface layer is calculated using the power-law profile

$$U(Z) = U_r\left(\frac{Z}{z_r}\right)^{\alpha} \quad (3)$$

where α is the power-law exponent calculated as (Sharan and Kumar, 2009)

$$\alpha = \frac{u_*}{\kappa}\frac{\phi_m(z_r/L)}{U_r} \quad (4)$$

in which κ $(=0.4)$ is the von Karman constant and ϕ_m is the stability function of momentum characterized by Z and L. We have considered $\phi_m(Z/L) = 1$ in the neutral

surface layer ($L \to \infty$). In convective atmospheric stability conditions ($L < 0$), $\phi_m\,(Z/L) = (1 - 16\,Z/L)^{-1/4}$ (Dyer, 1974). The effective wind speed at the effective height of the plume z_{eff} is taken as $U_{eff} = (U[z_{eff}]^2 + 2\sigma^2{}_v)^{1/2}$ (Qian and Venkatram, 2011). For low wind speeds, we also set a minimum value of 0.3 m s^{-1} for σ_v that is used to parameterize the Gaussian plume model.

3.1.2 | Adjoint of the Gaussian plume dispersion model

The inversions require the computation of modelled CH_4 mole fractions corresponding to observations for each possible release rate and location in a discretized space. For such a computation, the application of the Gaussian model to each possible rate and location can be much less efficient than the use of its adjoint model (Marchuk, 1995; Pudykiewicz, 1998; Sharan *et al.*, 2009). The adjoint of the Gaussian model can be used to compute the sensitivity of the mole fraction at a measurement location to the emissions at all potential source locations. Recombining these sensitivities provides the full relationship between the potential release rate and location and the corresponding simulation of the mole fractions with the Gaussian model. This adjoint can be described as the Gaussian model itself with inverted wind direction originating from the mole fraction measurement location (Pudykiewicz, 1998; Sharan *et al.*, 2009). It is used by the inversions based on fixed-point measurements.

With the assumptions corresponding to the Gaussian model and that are detailed in Section 3.1.1, the sensitivity of the average mole fraction simulated by this model at a measurement location (0, 0, z_{meas}) to the emission $e(X, Y, Z)$ at the coordinates (X, Y, Z) (for positive X and Z) in a Cartesian coordinate system where the X and Y axis are defined by the direction opposed to that of the effective mean wind, is given by

$$\frac{dC\,(0,0,z_{meas})}{de(X,Y,Z)} = \frac{1}{2\pi\sigma_Y\sigma_Z U_{eff}} \exp\left(\frac{-Y^2}{2\sigma_Y^2}\right) \times \left[\exp\left(\frac{-(z_{meas}-Z)^2}{2\sigma_Z^2}\right) + \exp\left(\frac{-(z_{meas}+Z)^2}{2\sigma_Z^2}\right)\right] \quad (5)$$

where σ_Y, σ_Z and other parameters are defined by Equations (1)–(4) as in Section 3.1.1, with U_{eff} being computed as $(U(Z)^2 + 2\sigma^2{}_v)^{1/2}$ for consistency (the effective wind in the Gaussian model corresponding to the wind at source height).

3.2 | Inversions using the fixed-points measurements

We use two different least-squares frameworks to formulate the inverse problem for the localization and the quantification of the unknown continuous point sources using the fixed-point measurements. Unlike the inversions based on the mobile data which use some strong assumptions regarding the actual source height (see Section 3.3), both of these frameworks attempt at deriving the effective release height (z_e) potentially higher than the source's actual height z_s due to the plume rise (Briggs, 1975). When using both types of data, in principle, there is a potential to distinguish between the injection height and the emission rate owing to variations in vertical diffusion that are accounted for in the Gaussian model depending on the time interval or wind sector. However, the relatively low number of observed parameters when using the mobile data (see Section 2.3) limits the ability to solve for the release rate and its horizontal and vertical location. The amount of information assimilated when using the fixed measurements is expected to support the derivation of all these parameters together. Furthermore, when using the fixed-point measurements, the effective wind speed driving the plume is taken as a function of the injection height, adding more constraint on the derivation of this parameter. The inversions aim to minimize the root sum squared (RSS) misfits between the averages of the observed and modelled mole fraction enhancements (above the background) in the plumes, with bins corresponding at each active station to either relatively short time windows of equal lengths or to sectors of wind directions. The modelled mole fractions are derived from simulations with the adjoint of the Gaussian model driven by effective wind directions derived from meteorological measurements. We did not manage to refine such a direction based on the mole fraction gradients across the active stations, due to the lack of measurement points across the plume. Depending on the version of the inversion (depending on mole fraction binning and averaging), the model effective winds are computed consistently as averages of meteorological data within the bins corresponding to (a) consecutive time windows of equal lengths, or to (b) sectors of wind direction.

For each controlled release, the inversion finds the optimal horizontal and vertical location and rate estimate by looping over all the potential source positions in a 3D fine discretization of the volume over the ATEX area. For each position, it computes the theoretical optimal rate minimizing the RSS misfits using the adjoint of the Gaussian model. The estimates of the release location and rate are taken as those providing the smallest RSS misfits

among the ensemble of optimal results gathered during the loop over all potential source locations.

3.2.1 | Definition of the observation vector

A usual strategy in inverse modelling when using continuous measurements from fixed points would be to average them over the whole duration of the releases (Sharan *et al.*, 2009). However, given the limited number of active stations within or at the edge of the plume during each release (up to seven), the use of such averages would hamper the ability to derive both the release location and rate. Therefore, we attempt to exploit the change in the wind direction during a release by analyzing variations in the CH_4 mole fractions at a given active station. We expect to triangulate the source location based on the change of mole fraction depending on the change of wind direction (Luhar *et al.*, 2014; Kumar *et al.*, 2021). A trade-off is made for the averaging scale between the need to average the data over sets that are large enough for a proper comparison to the Gaussian model and the attempt at catching the impact of variations of the mean wind.

The basis for the averaging of both the CH_4 mole fraction data and the corresponding meteorological data is the binning of the data at each active station over successive time windows of equal duration or over wind direction sectors. Schematic diagrams illustrating the binning of the data over time windows and over wind direction sectors are given in Figure S2a, b in the Supplementary information. Averaged values of meteorological and turbulence parameters are used to parameterize the adjoint of the Gaussian model, which simulates the sensitivity of the average mole fractions to emissions for the corresponding time window or wind sector.

Let $\boldsymbol{\mu} = (\mu_1, \mu_2, \dots, \mu_m)^{\mathrm{T}} \in R^m$ (superscript T defines the transpose of a vector/matrix) be the general notation for the observation vectors containing m averages of the binned mole fractions at the fixed active stations. $\boldsymbol{\mu}_{\mathrm{tw}}$ denotes observation vectors based on binning over N_t ($= D_{\mathrm{s}}/\Delta t$, where D_{s} denotes the total duration of the corresponding release) time windows of equal length Δt at each active station, and $\boldsymbol{\mu}_{\mathrm{ws}}$ the ones based on binning within the wind sectors at each active station. Δt is selected to be short enough to capture the most significant variations in the meteorological conditions and yet long enough to reach a quasi-steady-state distribution of the mole fraction average despite turbulence (one of the main assumptions used for the comparison to the Gaussian plume model). Based on previous atmospheric dispersion studies using Gaussian plume models (Hanna *et al.*, 1982; Hoinaski *et al.*, 2016), Δt = approximately 15 min is selected when $U_{\mathrm{r}} \geq 1.5\,\mathrm{m\,s^{-1}}$. This duration appears to be sufficient to limit the impact of turbulent patterns in the average mole fractions, and since tripods are within approximately 50–120 m of the potential release locations, it is reasonable to assume that the airflow is uniform and steady-state over such a duration in the absence of significative obstacles in TADI area. The direction of wind becomes more variable in low wind speed conditions. Therefore, a shorter time interval $\Delta t = 7$ min is considered for the corresponding releases.

The binning of the data over wind direction sectors is based on the binning of 1-min averaged wind directions during a release. The total number of bins is first defined as the rounding integer of the division of the release duration (in min) by approximately 7 min. The aim, again, is to ensure that corresponding mole fraction averages can be representative of a timescale that is long enough for a comparison to the Gaussian model, and to ensure that the corresponding computation of turbulent parameters for this model make sense. For the same reason, only bins of wind directions gathering at least four 1-min averages are selected for the inversion. Depending on the distribution of the wind directions and on the release duration, the number of selected bins of wind directions ranges between two and seven.

3.2.2 | Discretization of the space of solution for the location of the source and transport operator

Preliminary tests (not shown) led us to assume that, even accounting for the release exit velocity and temperature, the estimates of the injection height of releases do not exceed 8 m. Therefore, in order to define a set of potential locations for the releases on which the inversion framework loops, the volume of air above the ATEX zone (whose surface measures 40 m × 50 m) up to 8 m height is discretized with a 3D grid with 1 m horizontal resolution and 0.5 m vertical resolution. The grid cells of this 40 m × 50 m × 8 m volume are denoted $\mathbf{x}_i = (x_i, y_i, z_i)$, $i = 1, 2, \dots, N$.

With such notations, the link between a given estimate of the release location $\mathbf{x}$ and rate q and the corresponding simulation of the observation vector $\boldsymbol{\mu}^{\mathrm{mod}}$ is given by the Gaussian model and by the extraction of the average mole fractions from this model, denoted altogether h: $(\mathbf{x}, q) \rightarrow \boldsymbol{\mu}^{\mathrm{mod}} = h(\mathbf{x}, q)$. For a fixed release location, this operator becomes $\mathbf{h}_{\mathbf{x}}$, a linear function of q (Sharan *et al.*, 2009): $\mathbf{h}_{\mathbf{x}}$: $q \rightarrow \boldsymbol{\mu}_{\mathbf{x}}^{\mathrm{mod}} = q\mathbf{h}_{\mathbf{x}}$.

In order to find the optimal release rate and location minimizing the misfit to $\boldsymbol{\mu}^{\mathrm{o}}$, the measured $\boldsymbol{\mu}$, a solution

could be to compute $\boldsymbol{\mu}^{\mathrm{mod}}$ for a predefined ensemble of possible locations and rates with the Gaussian model. The non-linearity of h with respect to $\mathbf{x}$ would require us to loop over all of the predefined ensemble of possible locations. In order to save computations (see Section 3.1.2) and to avoid defining and discretizing the range of possible rates, for a given $\mathbf{x}$, we compute the adjoint $\mathbf{h_x}^{\mathrm{T}}$ of $\mathbf{h_x}$ and use it to solve the mathematical equation providing the optimal release rate (see below). $\mathbf{h_x}^{\mathrm{T}} = (h_{\mathbf{x1}}, h_{\mathbf{x2}}, \ldots, h_{\mathbf{xm}})$ gives the sensitivity of the average mole fractions $(\mu_1^{\mathrm{mod}}, \mu_2^{\mathrm{mod}}, \ldots, \mu_m^{\mathrm{mod}})$ to the value of the release rate q. All values $h_{\mathbf{xi}}$ for a given i but all $\mathbf{x}$ are derived from a single application of the adjoint of the Gaussian model, computing the sensitivity of μ_i^{mod} to the emissions at all potential source locations. Therefore, the inverse computations rely on m applications of the adjoint of the Gaussian model.

3.2.3 | The minimization process

Overall, the inversion looks for the minimization of the following cost function:

$$J^{\mathrm{fix}}(\mathbf{x}, q) = \left\| \boldsymbol{\mu}^{\mathrm{o}} - \boldsymbol{\mu}^{\mathrm{mod}} \right\|^2 = \left\| \boldsymbol{\mu}^{\mathrm{o}} - h(\mathbf{x}, q) \right\|^2 \qquad (6)$$

using the notation $\|\mathbf{v}\|^2 = \mathbf{v}^{\mathrm{T}}\mathbf{v}$ for a vector $\mathbf{v}$. The optimization approach is similar to that described in Sharan *et al.* (2012). For each grid cell $\mathbf{x}$, $J_{\mathbf{x}}^{\mathrm{fix}}(q) = J^{\mathrm{fix}}(\mathbf{x}, q) = \|\boldsymbol{\mu}^{\mathrm{o}} - q\mathbf{h_x})\|^2$ is minimized with respect to q in order to derive the optimal release rate $q_{\mathbf{x}}^{\mathrm{opt}}$. The minimum of the quadratic function $J_{\mathbf{x}}^{\mathrm{fix}}$ is found by solving for $\frac{\partial J_{\mathbf{x}}^{\mathrm{fix}}(q)}{\partial q} = 0$ that is,

$$q_{\mathbf{x}}^{\mathrm{opt}} = \frac{\mathbf{h_x}^{\mathrm{T}}\boldsymbol{\mu}^{\mathbf{o}}}{\left\|\mathbf{h_x}\right\|^2} \qquad (7)$$

The minimum value of J^{fix} (Equation 6) at $\mathbf{x}$ is given by

$$J^{\mathrm{fix}}\left(\mathbf{x}, q_{\mathbf{x}}^{\mathrm{opt}}\right) = J_{\mathbf{x}}^{\mathrm{fix}}\left(q_{\mathbf{x}}^{\mathrm{opt}}\right) = \|\boldsymbol{\mu}^{\mathbf{o}}\|^2 \left[1 - S(\mathbf{x})^2\right] \qquad (8a)$$

where

$$S(\mathbf{x}) = S_{\mathbf{x}} = \frac{\mathbf{h_x}^{\mathrm{T}}\boldsymbol{\mu}^{\mathbf{o}}}{\|\mathbf{h_x}\| \ \|\boldsymbol{\mu}^{\mathbf{o}}\|} \qquad (8b)$$

The minimum of $J^{\mathrm{fix}}(\mathbf{x}, q)$ is thus found by deriving the maximum of $S_{\mathbf{x}}$ with respect to $\mathbf{x}$.

In summary, the inversion loops over all $\mathbf{x}$ in the ensemble of possible source locations to derive corresponding values of $q_{\mathbf{x}}^{\mathrm{opt}}$ and $S_{\mathbf{x}}$, and it identifies the location $\mathbf{x}_{\mathrm{e}}$ providing the largest value for $S_{\mathbf{x}}$. $q_{\mathrm{e}} = q_{\mathbf{x}_{\mathrm{e}}}^{\mathrm{opt}}$ and $\mathbf{x}_{\mathrm{e}} = (x_{\mathrm{e}}, y_{\mathrm{e}}, z_{\mathrm{e}})$ are taken as the estimates of the release rate and location, respectively.

3.3 | Inversion method for mobile measurements

We use the same atmospheric inversion modelling framework as Kumar *et al.* (2021) for the localization and quantification of the releases, using the near-surface mobile mole fraction measurements. The rationale and the details for this approach are given in this previous publication and we just summarize them. Due to the very different information content of the data from the mobile measurements and from the fixed stations, we need to use some very different assumptions and slightly different targets when processing these two datasets. Here the inversion estimates the location and rate of a release using the integrals of the CH_4 mole fractions above the background in the N_{p} plume cross-sections from the mobile transects during a release. These integrals characterize the amplitudes of the plume cross-sections. The observed amplitudes are compared individually to the amplitudes simulated with the Gaussian model.

We conduct one simulation with this model per plume cross-section and per potential source location. For a potential source location and a simulation corresponding to the ith plume cross-section, we define the effective wind direction θ_{mi} as the direction from the potential source location to the 'centre' of the plume transect. In practice, the 'centre' of the plume transect is defined manually by analyzing the measurements. The effective wind speed at the actual source height (z_{s}) in the Gaussian model is systematically defined using the power-law profile detailed in Section 3.1.1, and the averages of the values of the meteorological and turbulence parameters over the release periods. In order to extract the amplitude of a plume transect from the Gaussian model, the mole fractions from this model are sampled at the measurement locations before being integrated along this plume cross-section in a way consistent with the computation of the observed amplitude. The method requires the availability of at least two plume cross-sections for a given release, exploiting the variations of the amplitudes as a function of the location of the plume cross-sections, and the variations of these locations to identify the source locations as well as the release rates.

Unlike inversions using the measurements from the fixed stations, inversions using mobile measurements do not attempt to derive the injection height of the source. This height is constrained using the known height of the release z_{s}. However, as for the use of the measurements from the fixed stations, the ATEX area is discretized with a 1 m horizontal resolution to define the ensemble of possible horizontal locations for the source $\mathbf{x}^{\mathrm{horiz}} = (x, y)$, over which the algorithm loops to identify the optimal one. Using the adjoint of the transport model would have been more difficult in this inverse modelling framework

since the observation vector is composed of a complex combination of instant mole fractions along the mobile transects and since the effective wind direction driving the Gaussian plume follows the direction between the potential source location and the centre of the plume cross-sections.

The inversion minimizes the relative misfits between the modelled and observed integrals of individual plume cross-sections, and between the measured average wind direction and the directions from the source location estimate to these individual plume cross-sections, that is, of the following cost function J^{mob} of the source location and rate (Kumar *et al.*, 2021):

$$J^{\mathrm{mob}} = J_p + J_w \tag{9}$$

where

$$J_p = \sum_{i=1}^{N_\mathrm{p}} \left[\frac{A_{\mathrm{o}i} - A_{\mathrm{m}i}}{A_{\mathrm{o}i}} \right]^2 \tag{10}$$

is the quadratic sum of relative errors between the modelled ($A_{\mathrm{m}i}$) and observed ($A_{\mathrm{o}i}$), amplitudes of the N_p plume cross-sections and

$$J_w = \sum_{i=1}^{N_\mathrm{p}} \left[\frac{\theta - \theta_{\mathrm{m}i}}{\sigma_\theta} \right]^2 \tag{11}$$

is the quadratic sum of the weighted departure from θ of the implicit effective wind directions $\theta_{\mathrm{m}i}$ corresponding to the N_p plume cross-sections.

Kumar *et al.* (2021) minimized J^{mob} (Equation 9) by iterating on all the predefined values of the potential locations and rates for the releases: a set of potential release rates was defined for this purpose. In order to reduce the corresponding level of computations and to avoid relying on a predefined set of potential release rates, here the minimization of J^{mob} is performed in two steps, in a way similar to the approach when using fixed-point measurements. In the first step, the optimal rates for each potential location ($\mathbf{x}^{\mathrm{horiz}}$) are estimated using $A_{\mathrm{o}i}$ and the amplitudes $R_{\mathrm{m}i}$ simulated with the Gaussian model forced with a unity emission rate (1 kg s^{-1}) as (see Appendix A):

$$q^{\mathrm{opt}}_{\mathbf{x}^{\mathbf{horiz}}} = \frac{\sum_{i=1}^{N_\mathrm{p}} \left(\frac{R_{\mathrm{m}i}}{A_{\mathrm{o}i}} \right)}{\sum_{i=1}^{N_\mathrm{p}} \left(\frac{R_{\mathrm{m}i}}{A_{\mathrm{o}i}} \right)^2} \tag{12}$$

In the second step, the algorithm loops over all possible source locations $\mathbf{x}^{\mathrm{horiz}}$ and compares the values of J^{mob} corresponding to $q^{\mathrm{opt}}_{\mathbf{x}^{\mathbf{horiz}}}$ to identify the global minimum of J^{mob}. The location $\mathbf{x}^{\mathbf{horiz}}_{\mathbf{e}} = (x_\mathrm{e}, y_\mathrm{e})$ or $\mathbf{x}_\mathrm{e} = (x_\mathrm{e}, y_\mathrm{e}, z_\mathrm{s})$ and the rate $q_\mathrm{e} = q^{\mathrm{opt}}_{\mathbf{x}^{\mathbf{horiz}}_{\mathbf{e}}}$ corresponding to the global minimum of J^{mob} are taken as estimates of the release location and rate, respectively.

Kumar *et al.* (2021) showed that Equations (9)–(11) implicitly assume a relative random model error when simulating the amplitude of individual plume transects of 100%. Kumar *et al.* (2021) also showed, in their application of the method to the measurement made during TADI-2018, that J^{mob} was dominated by J_w. As a result, the inversion system was not able to exploit the variations of the amplitudes from one plume cross-section to the other to identify the release location, and tended to locate this release at the upwind boundary of the ATEX zone to minimize J_w. They conducted tests giving more weight to J_p in Equation (9), that is, assuming that the model error could be very small, by artificially rescaling J_w. These tests highlighted a lack of constraint to derive the source location using J_p, whose cause was thought to be the lack of plume cross-sections. We attempt to apply the method with its default configuration here, assuming that the much larger number of plume cross-sections available for the releases during the TADI-2019 campaign should help to overcome this problem.

4 | RESULTS

4.1 | Evaluation of the model and inversion configurations using the known release rate and location

This section is dedicated to the evaluation of the skill of the model to simulate the values given by the measurements for the different observation vectors defined in Section 3 ($\boldsymbol{\mu}^{\mathbf{o}}{}_{\mathrm{tw}}$ and $\boldsymbol{\mu}^{\mathbf{o}}{}_{\mathrm{ws}}$ for the inversion using fixed-point measurements, and the $A_{\mathrm{o}i}$ when using the mobile measurements). The model is run with the known release rates q_s and locations $\mathbf{x}_\mathrm{s} = (x_\mathrm{s}, y_\mathrm{s}, z_\mathrm{s})$ and compared to these values. The aim is to provide some first insights into the reliability of the inverse modelling configurations regarding both the choice of the transport model and the definition of the observation vectors and cost functions to minimize. However, the reference inversion configurations are not adjusted based on information from such diagnostics, with data (the location and rate of the releases) which should be unknown in the inversion process.

4.1.1 | Model error when considering the fixed-point measurements

Figure 4 illustrates the results for release-1 with the fixed-point measurements when using both binning methods. The mean wind directions (θ) corresponding to a

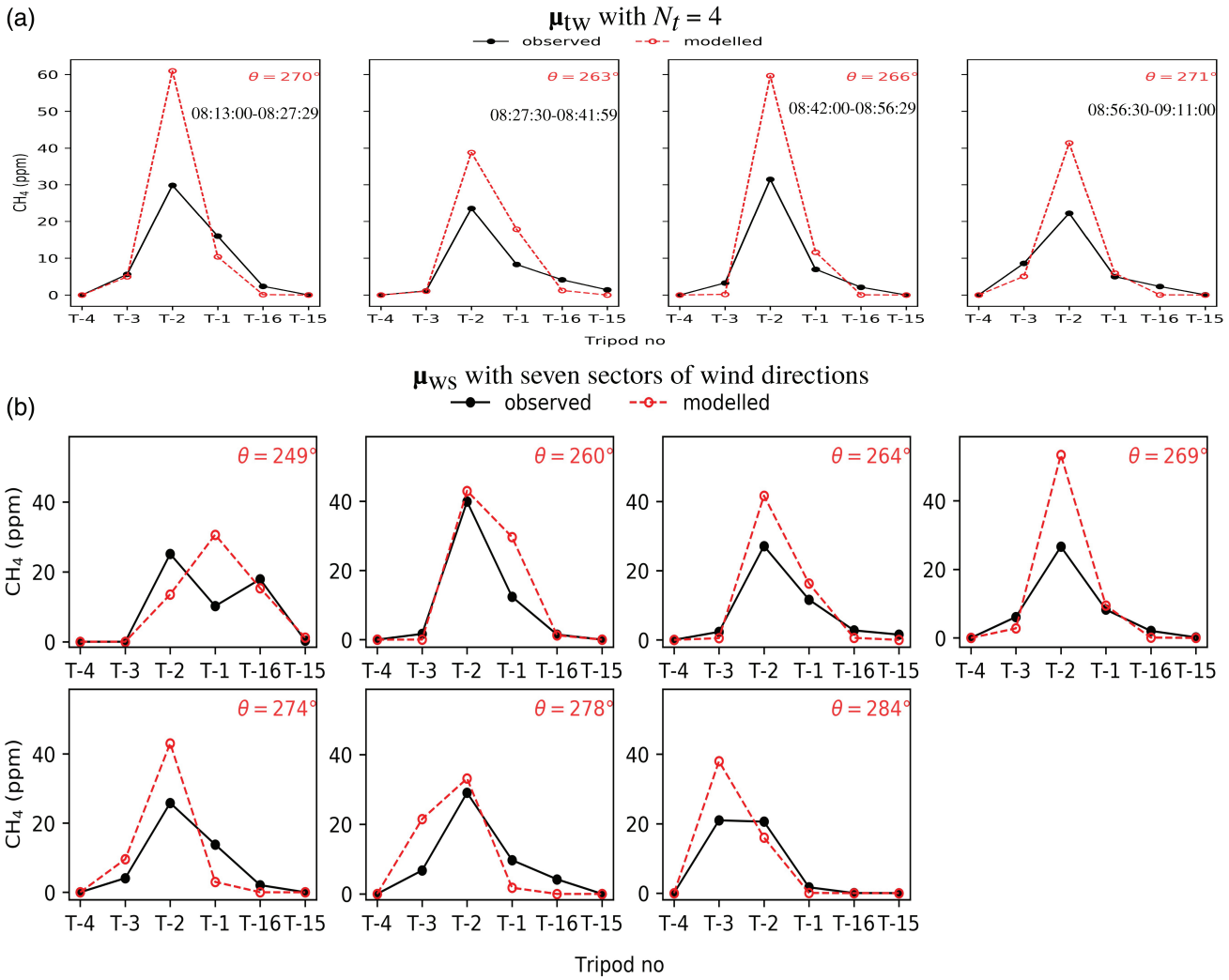

FIGURE 4 Observed and modelled (with known release location and rate) average CH_4 mole fractions for (a) $\boldsymbol{\mu}_{tw}$ (b) $\boldsymbol{\mu}_{ws}$ for release-1. The average wind direction θ corresponding to each binning period or sector is given on the top right of the plots [Colour figure can be viewed at wileyonlinelibrary.com]

given temporal bin or to a given bin of wind directions, is highly consistent with the direction from the release location to the tripod with maximum average mole fractions for this bin. In a general way, this consistency allows the model to produce average mole fraction variations across the active tripods that are well correlated with those from the measurements. However, the maximum values of the CH_4 mole fraction in each individual bin are generally overestimated by the model (Figure 4). Since the model also tends to underestimate mole fraction at the active tripods that appear to be located at the edge of the plumes, it generally produces average plumes that are narrower than observed. Overall, for all releases, the modelled mole fractions in each individual bin (whatever the binning method) are in good agreement with observations.

The least-squares inversion for fixed-points measurements minimizes the RSS misfits between the averages of the observed ($\boldsymbol{\mu}^{o}_{tw}$ or $\boldsymbol{\mu}^{o}_{ws}$) and modelled enhancements of CH_4 mole fractions at all the active tripods in all the bins of a given release. Therefore, the performance of the model for a release is quantified using the root mean square error (RMSE) between these observed and modelled enhancements when the model uses the known release rate and location. Since the emission rates vary depending on the releases in a wide range between 0.16 and 30 g CH_4 s^{-1} (Table 1), we compute a normalized RMSE (i.e., NRMSE) which is defined by normalizing the RMSE by the standard deviation of the observed averaged CH_4 mole fractions across all the active tripods in all the bins of a release. This normalization supports the comparisons of the scores of RMSE obtained from the different releases.

The NRMSEs for both binning methods are shown for all releases in Figure 5. The NRMSE values for release-1 (Figure 4) are 107% and 80%, respectively, for $\boldsymbol{\mu}_{tw}$ and $\boldsymbol{\mu}_{ws}$. For $\boldsymbol{\mu}_{tw}$, the NRMSE ranges from 32% (release-24) to 268% (release-22), with an average value of 102% over all 26

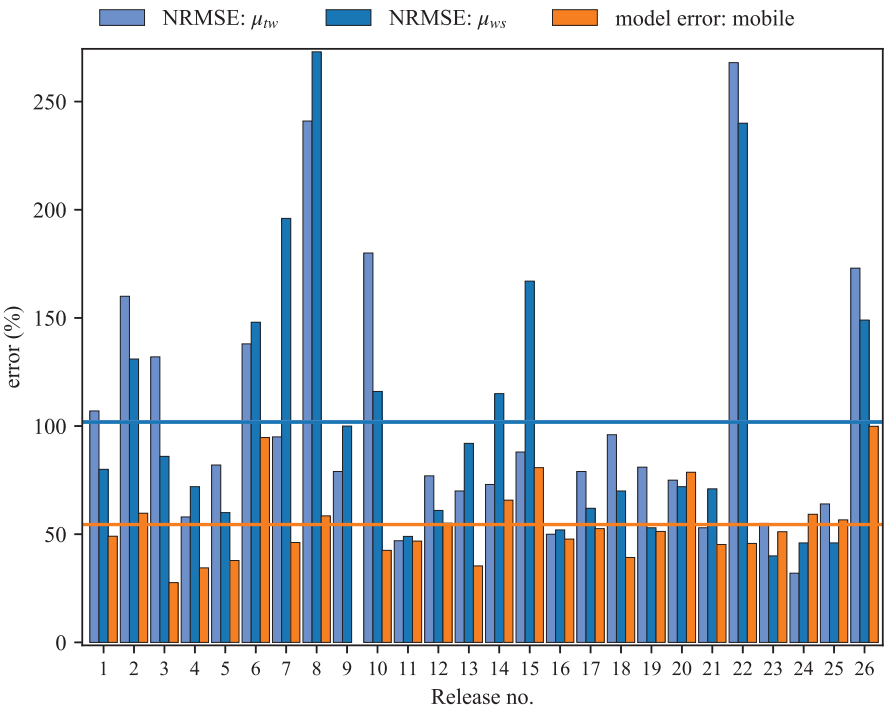

FIGURE 5 Model error when using the actual release location and rate for each release: Normalized root mean square error (NRMSE), expressed in percentage, between the modelled and the observed observation vectors $\boldsymbol{\mu}_{tw}$ and $\boldsymbol{\mu}_{ws}$ when using fixed-point measurements and the model errors (average of the absolute relative differences between the amplitudes of the observed and the simulated plume cross-sections) when using mobile measurements. The solid coloured lines indicate the average of the NRMSEs and model errors over all releases [Colour figure can be viewed at wileyonlinelibrary.com]

releases. Similarly, for $\boldsymbol{\mu}_{ws}$, the NRMSE ranges from 40% (release-23) to a maximum of 273% (release-8) (Figure 5), with an average value of 102% over all 26 releases. Even though the number of time windows and wind sectors for the respective binning methods and for a given release are generally very different, the NRMSEs corresponding to the two binning methods are very similar for almost all releases. Overall, the results show that the modelling capability is suitable for the inverse modelling framework using fixed-point measurements with both binning methods. We can expect similar performances from both inversion configurations.

4.1.2 | Model error when considering mobile measurements

The model error for the inversions using mobile measurements is defined consistently with the formulation of J_p (Equation 10) (Kumar *et al.*, 2021) as the average over all plume cross-sections during a release of the absolute value of the relative differences between the amplitudes of the observed and the simulated plume cross-sections when forcing the Gaussian model with a known release rate and location. This model error varies from approximately 27% (release-3) to approximately 100% (release-26) with an average value of approximately 54% for all the 25 releases. These values are generally much smaller than the 100% model error implicitly assumed by the formulation of J_p (see Section 4.2.3 and Kumar *et al.*, 2021). The default setup of the inversion configuration when using the mobile measurements can thus be seen as conservative: it allows departure from the observed plume amplitudes to exceed those obtained when using the actual release rates and locations. However, despite the better meteorological conditions during TADI-2019 than during TADI-2018, these model errors are similar to those encountered in Kumar *et al.* (2021). They continue to exceed the values artificially used by Kumar *et al.* (2021) to balance the weight of J_p and J_w in J^{mob}.

When using the actual source location, the deviation of the θ_{mi} from θ varies from 0.02° to approximately 108° with an average deviation of approximately 18° over all the plume cross-sections of all the releases. This is smaller than the average value of σ_θ (~20°) which varies between approximately 9° and approximately 48°. Again, the configuration of J_w can thus be seen as being conservative, allowing for departures from the measured wind that are larger than those obtained when using the actual release location. This partially balances the conservatism of the assumption on the model error in the formulation of J_p.

4.2 | Estimates of release rates and locations

The estimates of the rates and locations of the releases from all of the inversions (using fixed points or mobile measurements) are evaluated against the actual values. For

TABLE 2 Summary of inversion results using the fixed-points and the mobile measurements, and comparisons between the actual and the inverted source height and rates

	Actual source parameters		Inversions using fixed-point measurements								Inversions using mobile measurements		
			With data binned over the time windows (μ^o_{tw})				With data binned over the wind sectors (μ^o_{ws})						
No	z_s (m)	q_s (g s^{-1})	z_e (m)	q_e (g s^{-1})	Rel. error	E_l (m)	z_e (m)	q_e (g s^{-1})	Rel. error	E_l (m)	q_e (g s^{-1})	Rel. error	E_l (m)
1	0.96	10	0.5	6.36	36.35%	3.83	0.5	5.90	41.04%	3.80	10.74	7.35%	23.52
2	0.75	30	1.5	17.48	41.74%	12.71	0.5	16.25	45.83%	5.79	23.86	20.48%	23.52
3	0.39	1	0.5	1.23	23.23%	10.03	0.5	1.16	16.52%	4.76	0.95	4.92%	15.88
4	1.9	0.5	0.5	0.73	46.22%	2.70	0.5	0.57	13.88%	3.23	0.49	1.69%	24.00
5	2.5	5	0.5	6.57	31.47%	13.72	0.5	7.31	46.20%	6.69	7.92	58.47%	30.65
6	3	3	3.0	1.64	45.31%	20.00	2.0	1.50	49.93%	21.57	1.99	33.75%	43.44
7	0.61	1	1.5	0.88	11.99%	13.63	2.0	0.96	3.47%	18.16	1.07	7.27%	26.22
8	0.59	0.5	0.5	0.34	33.10%	11.81	0.5	0.43	14.52%	6.96	0.29	42.00%	17.54
9	1.9	0.16	0.5	0.20	21.69%	12.70	0.5	0.18	12.81%	5.08			
10	6	1	8.0	1.04	4.33%	1.40	6.5	0.89	11.47%	11.11	0.99	1.28%	12.40
11	2.22	2	1.0	2.92	45.98%	3.48	0.5	2.80	39.98%	3.65	2.37	18.62%	25.40
12	1.9	2	1.0	3.10	55.16%	9.61	1.0	2.52	26.14%	6.83	1.57	21.52%	31.61
13	2.44	4	2.5	4.76	18.97%	8.39	2.0	5.47	36.70%	10.58	3.53	11.68%	23.31
14	1.9	1	2.5	1.36	36.38%	8.22	1.0	1.31	31.06%	9.10	1.04	4.37%	48.99
15	1.9	1	0.5	0.46	53.91%	3.42	0.5	0.90	10.44%	15.56	0.96	4.18%	48.99
16	1.9	2	0.5	2.18	9.16%	6.36	0.5	2.23	11.65%	4.85	1.73	13.69%	27.39
17	1.83	5	1.0	6.80	36.01%	19.08	0.5	4.11	17.75%	5.95	4.62	7.55%	22.51
18	0.39	0.4	3.5	0.36	8.85%	13.94	0.5	0.34	16.08%	4.77	0.48	19.78%	32.88
19	1.26	0.5	0.5	0.82	64.54%	20.99	0.5	0.48	4.76%	0.50	0.45	10.73%	27.56
20	0.59	0.6	0.5	0.60	0.07%	4.53	0.5	0.57	5.18%	3.62	0.73	21.06%	43.79
21	2.22	1	3.0	1.40	39.53%	0.16	2.0	0.96	3.98%	4.59	1.97	96.65%	37.88
22	6	2	8.0	1.48	26.08%	15.89	7.5	1.65	17.35%	14.29	2.03	1.70%	53.09
23	0.39	4	0.5	5.32	33.06%	10.91	1.0	6.36	59.06%	10.56	4.40	9.98%	11.85
24	1.29	2	1.5	3.09	54.28%	9.91	0.5	2.04	1.75%	2.88	1.39	30.52%	22.32
25	0.59	2	0.5	2.62	30.80%	4.41	0.5	2.08	4.27%	2.72	1.79	10.59%	28.32
26	0.61	0.5	8.0	0.44	12.06%	15.35	0.5	0.17	65.78%	14.43	0.29	41.01%	17.71
MEAN					31.55%	9.89			23.37%	7.77		20.03%	28.83

each release, the horizontal location error (E_l) is defined as the Euclidean distance between the inverted $\left(\mathbf{x}_e^{horiz}\right)$ and actual $[(\mathbf{x}_s^{horiz} = (x_s, y_s)]$ horizontal source locations, and the relative error in the emission rate is computed as the ratio between the absolute value of the estimation error and the actual emission rate (Table 2). We also analyze the difference between the estimates of the injection heights when using fixed-point measurements with the actual release heights. This difference, if explained as expected by the exit velocity and temperature of the releases, should be positive. Figure 6 shows the ratios between the estimated (q_e) and actual (q_s) emission rates for all of the inversions.

4.2.1 | Results when using fixed-point measurements and $\boldsymbol{\mu}_{tw}$

Results from the inversions using fixed-point measurements and the observation vector $\boldsymbol{\mu}_{tw}$ are illustrated by

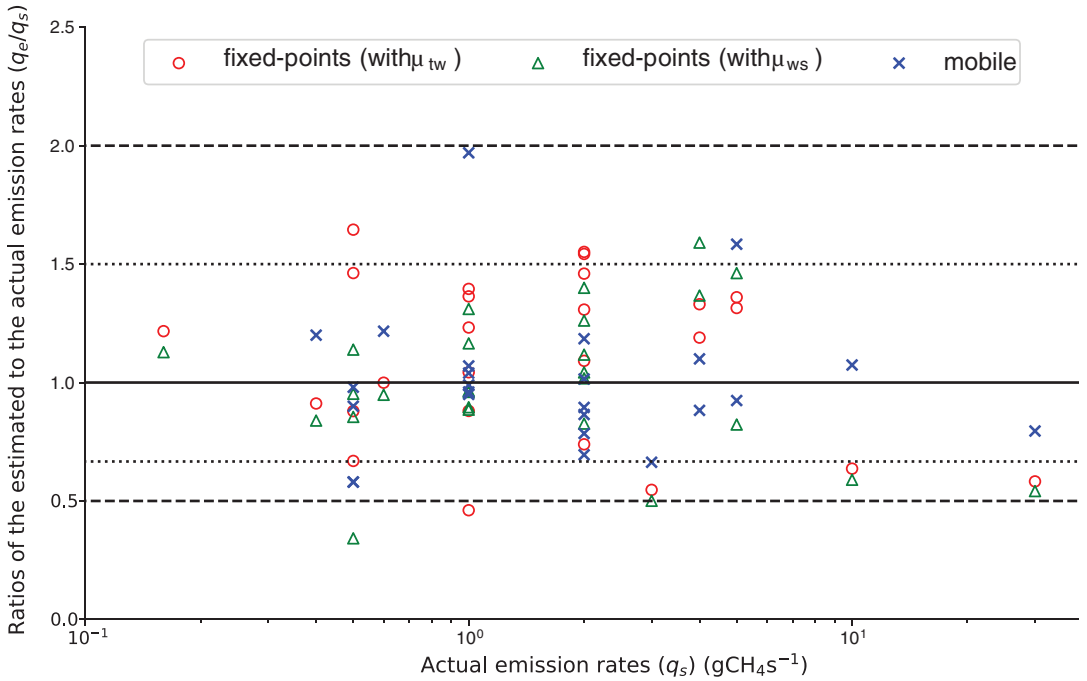

FIGURE 6 Ratios of the estimated to the actual emission rates (q_e/q_s) for the three sets of inversions using the fixed-points (with two versions of the observation vector) and mobile measurements. The solid line is the one-to-one line whereas the dotted and dashed lines correspond to a factor of 1.5 and 2 respectively, relative to the actual (q_s) emission rates [Colour figure can be viewed at wileyonlinelibrary.com]

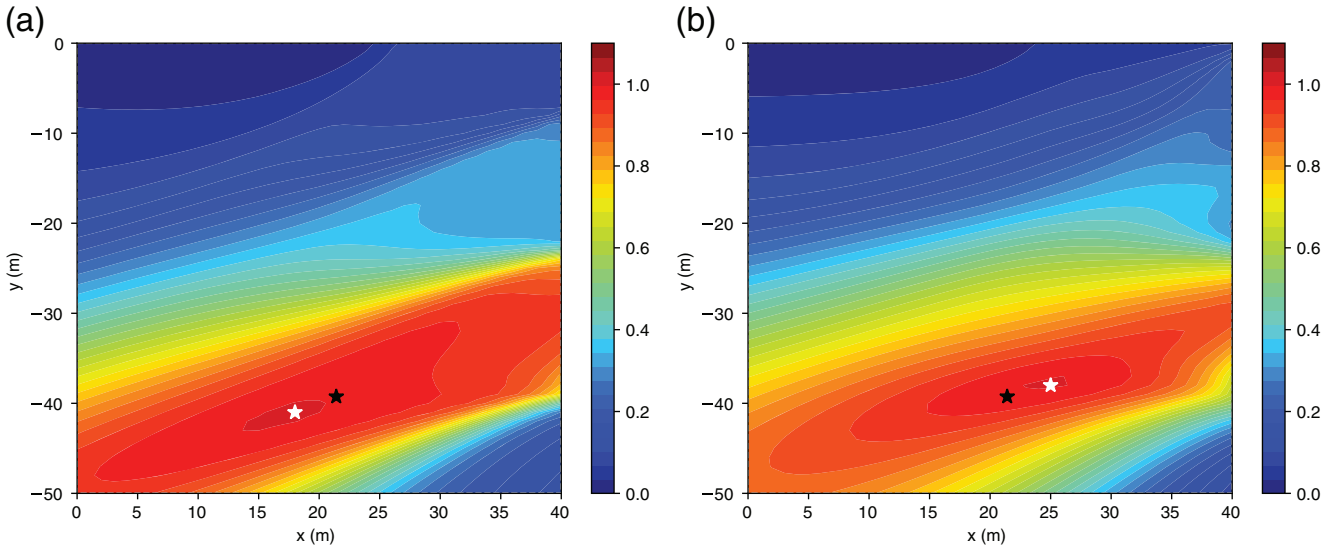

FIGURE 7 Contours of the function $S_{\mathbf{x}}$ (normalized by its maximum value) as a function of $\mathbf{x}^{\text{horiz}}$ in the ATmosphere EXplosive (ATEX) area when fixing z to z_e; results from the inversions with (a) $\boldsymbol{\mu}_{\text{tw}}$ and (b) $\boldsymbol{\mu}_{\text{ws}}$ for release-1. Black and white stars respectively show the actual and estimated locations of this release [Colour figure can be viewed at wileyonlinelibrary.com]

those from release-1 (Figures 7a and 8). The release rate estimate for this release-1 is 6.36 g CH_4 s^{-1} and should be compared to the actual rate of 10 g CH_4 s^{-1}: the error is approximately 36%. Figure 7a gives the shape of the function $S_{\mathbf{x}}$ when fixing z to z_e, the optimal release height estimate given by the inversion. A clear maximum is found near the actual source location. Here, the variability of the wind direction allows the system to provide a precise estimate of source location with an error of approximately 3.8 m. The contours of $S_{\mathbf{x}}$ for all releases are illustrated in Figures S3.1 and S3.2 in the Supplementary information.

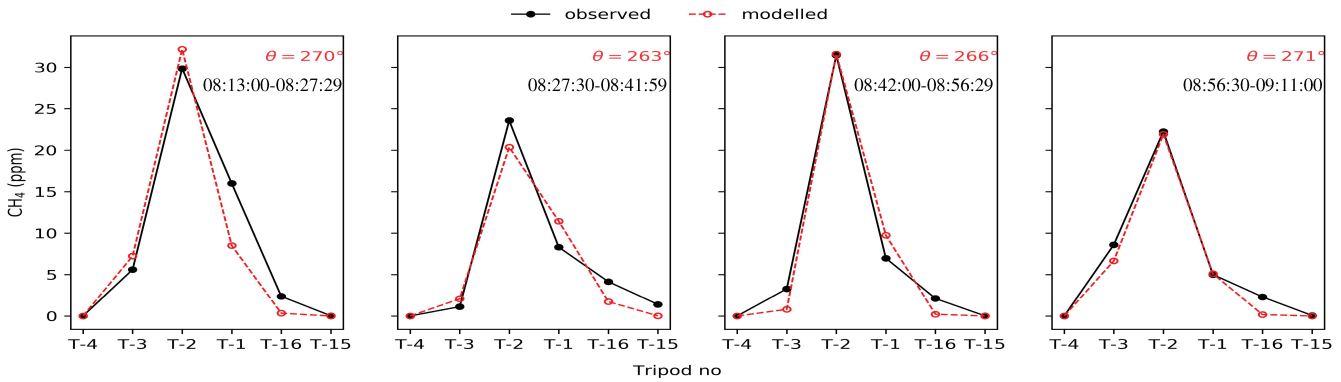

FIGURE 8 Observed and modelled CH_4 average mole fractions at all of the active tripods in each bin when using $\boldsymbol{\mu}_{tw}$ for release-1. Modelled average mole fractions are computed using $\mathbf{x}_e$ and q_e [Colour figure can be viewed at wileyonlinelibrary.com]

Figure 8 compares the observed and modelled (using $\mathbf{x}_e$ and q_e) average CH_4 mole fractions at each active tripod location across the plume for the different bins of $\boldsymbol{\mu}_{tw}$. It illustrates a good agreement between the observed and modelled average mole fractions, with a NRMSE of approximately 24%. This NRMSE is much smaller than the approximately 107% NRMSE obtained using the known release rate and location in the model. When considering all the 26 releases, the NRMSE ranges from approximately 4% (release-22) to 103% (release-3), with an average value of approximately 43% over all releases. The smaller NRMSEs obtained when using $\mathbf{x}_e$ and q_e than when using $\mathbf{x}_s$ and q_s is the result of the overfit of the data by the inverse modelling framework. Part of the model error is projected into the estimate of the release rate and locations rather than being interpreted as noise in the comparison between the modelled and observed average mole fractions.

Using $\boldsymbol{\mu}_{tw}$, approximately 96% of all the release rate estimates are within a factor of two of the actual emissions (Figure 6, Table 2). The relative error of these estimates ranges from 0.07% (for release-20) to 64.5% (for release-19), with an average value of 31.5%. The location error ranges from 0.16 to 21.0 m, with an average value of 9.9 m, which appears to be a moderate error given the size of the ATEX zone. For almost all releases, $\mathbf{x}_e$ is located within the ATEX zone (i.e., not at the border of this zone). This indicates that the results would have probably been the same if allowing the solution to be found outside the ATEX zone. Ignoring the seven releases corresponding to low wind speed conditions, the average relative error in the emission rates is 33.5% and the average location error is 10.5 m. Therefore, wind speed does not appear to be the main driver of the precision of the estimation. Notably, in approximately 50% of cases, injection height estimates are smaller than z_s (Table 2).

Several tests using $\boldsymbol{\mu}_{tw}$ in which we fix the injection height to the actual source height, and/or the horizontal location of the release to the actual one, are conducted to assess the robustness of the inversions and the ability to quantify the release rate from a known source location (Sharan *et al.*, 2009; Kumar *et al.*, 2021). When fixing the horizontal and vertical location of the source in the model to its actual location $\mathbf{x}_s$, the emissions are estimated within a factor of two of the actual emissions for approximately 77% of releases and the average relative error in the release rate estimates is approximately 32%. This is comparable to an average error of approximately 31% obtained when optimizing both the source location and rate. When fixing z_e to z_s, but optimizing the horizontal location together with the release rate, the average location error is 10.4 m and is thus comparable to that when optimizing z_e along with the horizontal source location and rate. However, the average relative error in the estimates of the emission rates increases to approximately 37%. Furthermore, fixing the horizontal location to $\mathbf{x}_s^{horiz}$ and optimizing both the release rate and height yields the best results in terms of release rate estimate with an error of approximately 27%. These results could be interpreted as a need to account for actual injection height but since z_e is often smaller than z_s, it should more likely be interpreted as a need to compensate for a bias in the vertical dispersion of the Gaussian model (Kumar *et al.*, 2021). Overall, this ensemble of results confirms that better release rates are obtained when fixing the horizontal location of the source to its actual position.

4.2.2 | Results when using fixed-point measurements and $\boldsymbol{\mu}_{ws}$

The results when using $\boldsymbol{\mu}_{ws}$ appear to be better than those obtained using $\boldsymbol{\mu}_{tw}$ (Figure 6, Table 2). Figure 7b shows the shape of $S_{\mathbf{x}}$ when fixing the source height to z_e for release-1 when using $\boldsymbol{\mu}_{ws}$ (Figures S4.1 and S4.1 in the

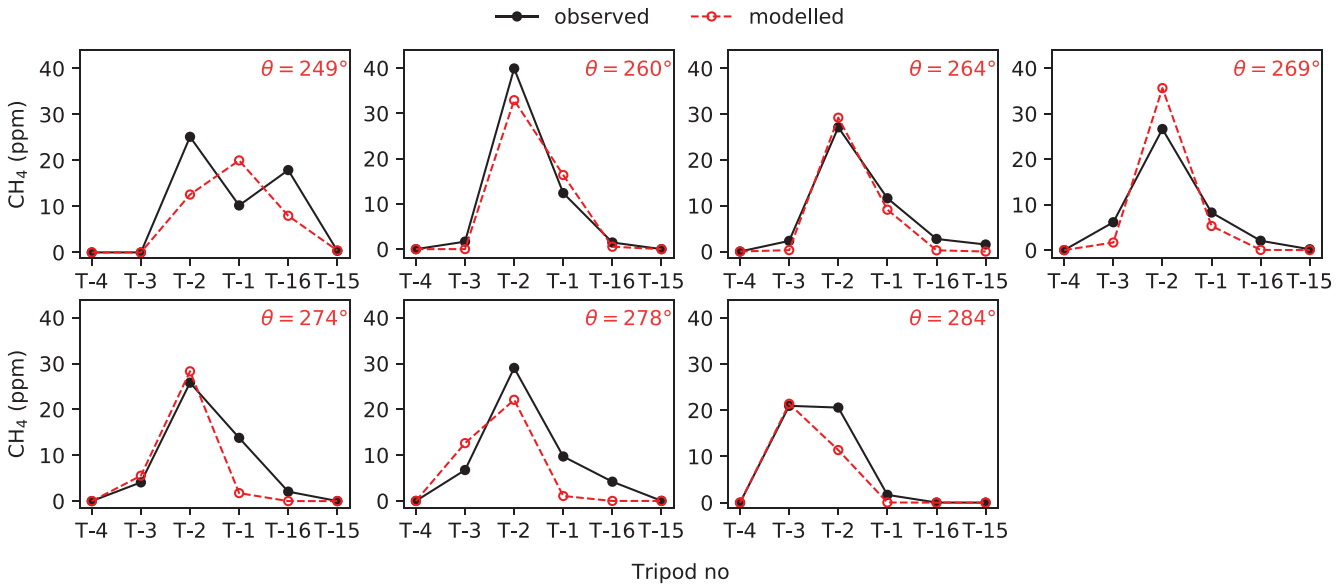

FIGURE 9 Observed and modelled (using $\mathbf{x}_e$ and q_e) average CH_4 mole fractions in each bin corresponding to sectors of wind direction at each tripod location for release-1 [Colour figure can be viewed at wileyonlinelibrary.com]

Supplementary information show $S_{\mathbf{x}}$ when z is fixed to z_e for all the releases). Seven wind sectors are used for $\boldsymbol{\mu}_{ws}$ in release-1 during which the averaged wind direction varied across a wide range of values from 249° to 284° (Figure 9). The observed and modelled (using $\mathbf{x}_e$ and q_e) CH_4 mole fractions are in good agreement at all tripods and in all the bins of the wind direction sectors (Figure 9). The source is estimated within less than 4 m downwind to the actual source location (Figure 7b). The emission rate is estimated as 5.90 g CH_4 s^{-1} with a relative error of approximately 41% from the actual rate (Table 2). The NRMSE between the observed and modelled CH_4 mole fractions with $\mathbf{x}_e$ and q_e for this release-1 is approximately 46%, which is smaller than the approximately 80% NRMSE obtained using $\mathbf{x}_s$ and q_s in the model.

When considering all 26 releases, the relative error in the estimated emissions varies from 1.75% (release-24) to 65.8% (release-26) (Table 2), with an average value of 23.4%. In almost all of the releases (approximately 96%), emissions are estimated within a factor of two of the actual emissions. In only one release (release-26) corresponding to low wind speed conditions, the release rate is underestimated within a factor of three of the actual emission (Figure 6, Table 2). The location errors vary from 0.50 m (release-19) to 21.6 m (release-6) with an average value of 7.8 m, which appears to be relatively precise. Ignoring the seven releases corresponding to low wind speed conditions, the average relative error in the release rate estimates is 22.6% and the average location error is 6.5 m. The average value of NRMSEs between the observed and modelled CH_4 mole fractions corresponding to $\boldsymbol{\mu}_{ws}$ using $\mathbf{x}_e$ and q_e for all releases is approximately 46%, which is smaller than the approximately 102% average NRMSE obtained with $\mathbf{x}_s$ and q_s. This indicates an overfit of the observations that is similar to that when using $\boldsymbol{\mu}_{tw}$.

Tests when fixing the horizontal location of the release and/or its height to their actual values lead to similar conclusions, albeit with significant differences between when using $\boldsymbol{\mu}_{ws}$ and when using $\boldsymbol{\mu}_{tw}$. Fixing the horizontal location to $\mathbf{x}_s^{horiz}$ leads to a similar average error in the release rate estimate (~30%) when the release height is fixed to z_s or an increase of it when the release height is optimized from approximately 23% to approximately 29%. Fixing the release height to z_s increases the average error from approximately 23% to approximately 30% or approximately 29% when optimizing or fixing the horizontal location of the source. Again, since z_e is often smaller than z_s in these cases, this should be seen as a compensation for a bias in the vertical diffusion of the Gaussian model rather than the impact of the need to account for the vertical rise of the plume exiting the source at z_s. Notably, when fixing the release height to z_s and optimizing the horizontal location of the source, the average location error (7.6 m) is comparable to that obtained when optimizing this height together with the horizontal location and rate of the release.

4.2.3 | Results using the mobile measurements

The results of the inversions using mobile measurements are presented in Table 2. As an example, Figure 10 shows the shapes of J^{mob} and of its components, J_p and J_w, as

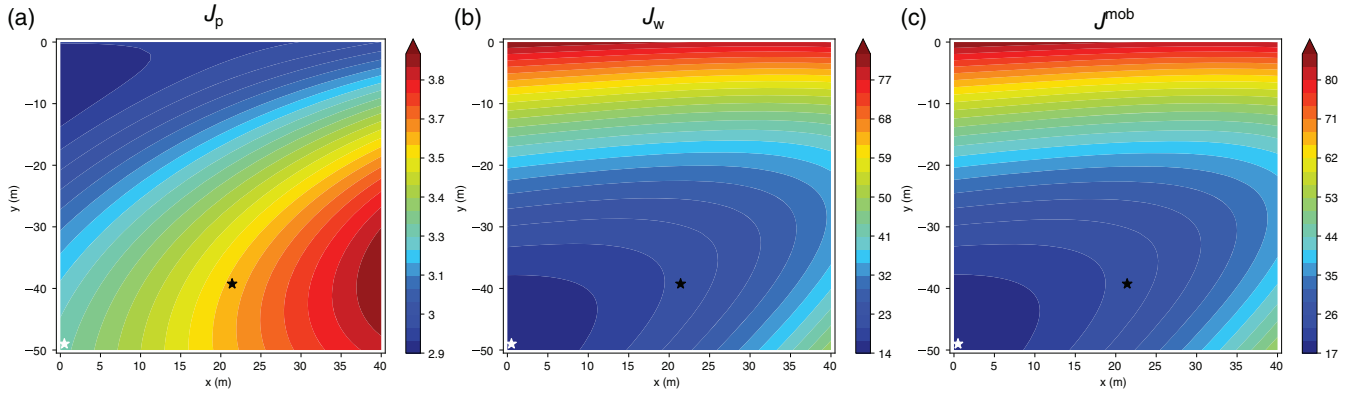

FIGURE 10 Contour plots of (a) J_p, (b) J_w, and (c) J^{mob} when fixing q to q_e for release-1. Black and white stars show respectively the actual and inverted source locations [Colour figure can be viewed at wileyonlinelibrary.com]

a function of the estimate of the source horizontal location $\mathbf{x}_e^{horiz}$ when fixing q to q_e from the inversion for release-1 (Figures S5.1 to S5.5 of the Supplementary information show this for all releases). This figure illustrates the dominant role of the minimization of J_w for the localization of the releases as in Kumar *et al.* (2021). This applies to all releases, and as in Kumar *et al.* (2021), this leads to the location of the source at the border of the ATEX area and to relatively large location errors ranging from approximately 12 m to approximately 53 m with an average value of approximately 29 m. However, in all the 25 CH_4 releases for which mobile measurements are available, the emission rates are estimated within a factor of two of the actual emissions. In fact, in approximately 88% of the releases, emissions are estimated within a factor of approximately 1.6. The relative error in the emission rate estimates in these tests ranges from approximately 1% (release-10) to 97% (release-21) with an average relative error of approximately 20%. Ignoring release-21, which corresponds to the largest error in the release rate estimate, this average relative error decreases to approximately 17%.

The average misfits between the amplitudes of the observed and the simulated plume cross-sections using $\mathbf{x}_e$ and q_e in the model vary from approximately 22% (release-26) to approximately 68% (release-15) with an average value of approximately 43% for all 25 releases. This is smaller than but close to the approximately 54% model error when using $\mathbf{x}_s$ and q_s, despite the relatively large relative location error. The sensitivity to the location of the source within the ATEX zone of the fit to the observed amplitude of the cross-sections appears to be relatively weak. The average of this absolute relative difference between the amplitudes of the observed and simulated cross-sections using $\mathbf{x}_e$, and q_e over all the plume cross-sections from all releases is approximately 45%. Furthermore, this average value of the misfits is comparable to the approximately 43% average misfit over all of the plume cross-sections from all the seven releases obtained in Kumar *et al.* (2021).

When fixing the location of the release to $\mathbf{x}_s$, the relative error in the release rate estimates ranges from approximately 3% (release-23) to approximately 61% (release 15, under low wind speed conditions), with an average value of approximately 30%. Ignoring the seven releases under low wind speed conditions which correspond to the seven largest relative errors, this average value decreases to approximately 24%. Unlike what is observed when using the fixed-point measurements, but as observed in Kumar *et al.* (2021), and even though the results obtained here are more precise than those from this study, the release rate estimates based on the mobile measurements are thus improved when fixing the release location to its actual position rather than optimizing it. This should be explained by model biases.

As in Kumar *et al.* (2021), we analyzed the results when giving more weight to J_p in J^{mob}, following the same procedure, that is, by recomputing ${J_\lambda}^{mob} = J_p + \lambda J_w$ with λ varying from approximately 10^{-5} to 1.0 even though it should reflect the level of model error. Figure 11 synthetizes the corresponding results. The location error appears to be weakly sensitive to λ. Even when ${J_\lambda}^{mob}$ is dominated by J_p, and thus when optimizing the release location mainly based on the variations of the amplitude of the plume cross-sections as a function of their location, this location is not precise. Crossing the source of information brought by these variations (reflected by J_p) and that of the measured wind direction (reflected by J_w) does not significantly improve the results. The optimal values for the error in the release rate and location estimates are obtained for $\lambda = 0.008$ but this corresponds to an unrealistically low model error of approximately 9%.

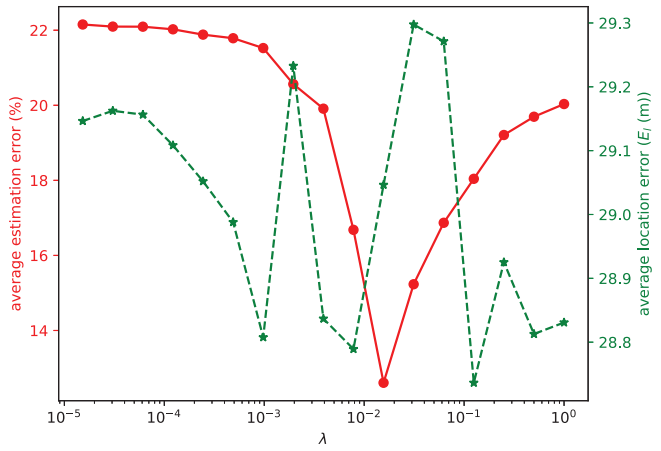

FIGURE 11 Average errors in the emission rates (solid line on left y-axis) and locations (dotted line on right y-axis) for all the releases with respect to λ in the cost function $J_\lambda{}^{\mathrm{mob}} = J_\mathrm{p} + \lambda J_\mathrm{w}$ [Colour figure can be viewed at wileyonlinelibrary.com]

5 | DISCUSSION

We evaluated two different types of atmospheric inversion frameworks for the monitoring of CH_4 emissions from industrial sites and facilities. They are based on stationary and near-surface mobile CH_4 mole fraction measurements and on a local-scale atmospheric dispersion model. In all the cases, using fixed or mobile data measured at various distances, and any of the specific inversion configurations proposed here, the inversions provide precise rate estimates for most of the releases. The average of the relative errors in the estimates of the wide range of CH_4 release rates tested during the TADI-2019 campaign typically ranges (depending on the inversion configuration) between approximately 20% and approximately 30%. Using the mobile measurements provides a slightly better estimate of the emission rates than using the stationary measurements with both observation binning approaches, with average relative errors of approximately 20% and approximately 23%–30% respectively. However, the source location is more precise when using the continuous measurements from fixed stations than when using mobile measurements, with an average location error of approximately 8–10 m and approximately 29 m respectively. The inversion tests constraining the source location in the model to the actual position of the release and using the mobile or fixed-point measurements also yield approximately 30% average relative error in the emission rate estimates.

The results indicate that the use of both approaches to bin the fixed-point measurements is suitable for both localization and quantification of the sources. The relative errors in the release rates estimated from the inversions using the fixed-point measurements do not show a correlation with the durations of the releases during the campaign (Figure S6a). This precision on the release rate estimates is smaller than 30% for the shortest releases, of 20 to 35 mins duration, when using both binning approaches. However, the location errors from the inversions with both binning approaches of the fixed-point measurements tend to decrease with longer releases (Tables 1 and 2, Figure S6b). With longer releases, strengthening the measurement constraint and the occurrence of more samples of the sectors of wind direction support a better triangulation of the source location. Release durations of more than 40 mins appear to be required for an estimate of the source location with errors smaller than approximately 10–15 m. Of note, this correlation between the precision of the release location estimates and the duration of the releases is slightly weaker when binning the observations according to the wind direction sectors than according to sequences of temporal windows. By source reconstructions, the inversions using the averaged mole fractions and atmospheric meteorological and turbulence data over bins corresponding to successive time windows of equal duration, assimilate more data during longer releases. The binning according to wind sectors can tend to select the data from long releases over the dominant sectors of wind directions so that the increase of the number of assimilated data for longer releases will be smaller than with the other binning. Another drawback of binning according to the wind sectors is that averaging data for a given wind sector over a long release may mix data corresponding to very different turbulence conditions. In principle, the approach should apply only to releases with approximately steady turbulence conditions. Accordingly, the inversion method using $\boldsymbol{\mu}_{\mathrm{ws}}$ is suitable for estimating releases over a duration on the order of 1 hr or less, but may not be so well suited for longer inversions.

The relative errors in the estimates of the release rates from the inversions using mobile measurements are generally smaller when acquiring more plume cross-sections in the measurements, and the number of plume cross-sections generally increases with longer releases (Figure S6c). For 18 out of the 19 releases during which we have at least nine plume cross-sections, the average relative error in the emission rate is approximately 11%, which is much smaller than the approximately 20% average relative error over all releases. This approximately 11% average error is also much smaller than the approximately 31% average error obtained in Kumar *et al.* (2021) for seven brief CH_4 releases with a small number (two to four) of plume cross-sections. The results confirm the natural assumption that having a larger number of plume cross-sections that can be extracted from the mobile measurements during longer releases yields more robust estimates of the emission rates. This partly explains why

we obtain an approximately 30% average error in the emission rate estimates when fixing the source locations to their actual locations whereas Kumar *et al.* (2021) had an approximately 44% average relative error for seven brief CH_4 releases.

However, in our inversions, the location error does not decrease when encountering more plume cross-sections (Figure S6d), opposed to what was assumed in the discussions of Kumar *et al.* (2021). The level of errors and the problems encountered for the localization of the releases (such as the location of releases at the border of the ATEX zone) in the inversions using the mobile measurements here are similar to those documented by Kumar *et al.* (2021) for much shorter releases. As in Kumar *et al.* (2021), we conducted inversions using the mobile measurements where we ignore the J_w term in the cost function, taking $J^{mob} = J_p$. This led to the same issues as those encountered with such tests in this study, even though it was assumed that a cost function J_p based on a large number of plume cross-sections should, in principle, support a robust triangulation of the source location. We acknowledge a lack of understanding of this problem, but these results support the assumption that the dispersion errors with the Gaussian model are the main explanation for the lack of ability to localize the releases with our inverse modelling framework when using the mobile measurements. The quantification and analysis of the model errors proposed in Section 4.1.2 implicitly assumes that these errors are completely random from one plume cross-section to the other, but the model likely bears biases.

An analysis of the relative errors in estimated emission rates with respect to the NRMSEs (for fixed points) or model errors (for mobile measurements) shows that the errors in estimated rates have a negligible correlation with the NRMSEs or model errors (Figure S7a, c). However, better estimations of the source locations are obtained with smaller values of NRMSEs or model errors in the inversions using fixed points or mobile measurements (Figure S7b, d). For fixed-point measurements, the location errors for inversions using $\boldsymbol{\mu}_{ws}$ have higher correlation with the NRMSEs compared to the inversions using $\boldsymbol{\mu}_{tw}$ (Figure S7b). These results highlight a clear link between the problem of the localization of the source and the model errors.

The impact of the model error is further highlighted when fixing all or part of the release location. First, the release rate estimates based on the mobile data are more precise when optimizing rather than fixing the source's horizontal location (see Section 4.2.3). Second, the tests of sensitivity to the optimization of the vertical injection height when using the fixed-point measurements yield estimates of the injection heights smaller than the actual release heights (see Sections 4.2.1 and 4.2.2). Even though such an optimization does not significantly impact the horizontal localization of the sources, this demonstrates that the model can have significant biases. Actually, such a conclusion applies to inversions with the optimization of z_e along with the source's horizontal locations and rates when using mobile measurements, even though we assumed that adding an unknown to the inversion problem when using the mobile data would be problematic. In such experiments, the average location error is 28.8 m for all 25 releases, which is comparable to the 28.8 m average error obtained when z_e is fixed to z_s. The relative errors in the emission rates for most of the releases are also approximately similar to those obtained when fixing z_e to z_s. Again, in these tests, many of the estimates of z_e fall below the actual release heights z_s. The problem is not related to the vertical resolution nor to the vertical extent of the grid used to derive z_e: the shapes of the cost functions as functions of z_e (once fixing the release horizontal locations and rates) are smooth and with a single local minimum, and the optimizations systematically localize the sources below 8 m height. Furthermore, we have conducted tests with finer (0.25 m) and coarser (1 m) vertical resolutions for this grid and the results were very similar (not shown). Notably, the wind shear near the ground surface is large, so that accounting for the variations of the wind speed on the vertical (simulated with the power-law profile — Equation 3) plays an important role in the inversions. For example, the average errors of the release rate and location estimates increase respectively from 23.4% and 7.8 m to approximately 48% and approximately 9 m in inversions using fixed-point measurements and $\boldsymbol{\mu}_{ws}$, deriving z_e and fixing U_{eff} in Equations (2a–c) and (5) to $[U(Z = 5\,\text{m})^2 + 2\sigma^2{}_v]^{1/2}$ with the averaged observed wind speed $U(Z = 5\,\text{m})$ at 5 m in each bin. Considering the relative simplicity of Equation 3, the lack of the wind vertical profile in the measurements, and more generally of different meteorological measurement points to characterize the 3D meteorological field, this highlights an important source of modelling uncertainty.

While demonstrating the presence of model biases, these tests do not provide a direct explanation for the high location errors when using mobile data. The comparison of the Gaussian plume model, which aims at modelling average dispersion fields, to near instantaneous plume cross-sections in the inversions using mobile data (while this model is properly compared to mole fraction averages in the inversions using data from fixed stations) probably provides a good theoretical link between the model errors and this problem. A last hypothesis could be that model errors become more problematic when applying a Gaussian model to mobile data measured much further from the source than the measurements from the fixed stations.

The inversions using a limited number of fixed measurement stations provide good estimates of both the location and rate of the releases, but we expect that denser networks of fixed sensors could support a more precise and robust monitoring of emissions. As discussed in Kumar *et al.* (2021), and supported by our new discussions on the impact of the modelling errors, another perspective for the improvement of flux estimates should be the use of a complex dispersion modelling system that could account for spatial and temporal wind variations and for vertical profiles of mole fraction, especially when deriving source locations with the mobile measurements. Finally, one of the main objectives of this study was to compare the observation and inversion frameworks relying on fixed-point and mobile measurements, but the concept of combining both types of measurements in a single inversion framework opens many perspectives. Various approaches could be considered such as using one dataset to refine the model configuration and the other for constraining the release location and rate estimates, or one dataset to localize the release and the other to derive the release rate, considering the strength and weaknesses of each dataset and of their respective treatment, if not, ultimately, constraining simultaneously the location and rate of releases based on both datasets. However, instead of highlighting some complementarities between the two types of datasets, our inverse modelling frameworks promote the choice of one type of measurements based on a trade-off between logistical constraints and the expectation for the estimates in terms of precision.

6 | CONCLUSIONS

This study presents local-scale inversion frameworks for the localization and quantification of methane releases using either mobile or fixed-point CH_4 mole fraction measurements. The inversions are tested during the TADI-2019 campaign with 26 controlled releases of 0.16 to 30 g CH_4 s^{-1}, lasting between 25 and 75 mins. The measurements were simultaneously taken near the surface around the release area at fixed points and from a mobile vehicle. All inversion approaches rely on a Gaussian plume dispersion model: in 'retro-transport' (adjoint) mode when using the fixed-point measurements and in forward mode when using the mobile measurements.

When using the fixed-points measurements, the estimate of the emission rates and locations corresponds to the least-squares minimization of the misfits between the modelled and measured average mole fractions. In order to maximize the number of fixed points of high-precision measurements across the plumes from the CH_4 releases, a system of switching the available limited number (6–7) of high-precision gas analyzers between a higher number (16) of different sampling lines depending on the wind direction was put in place during the campaign. However, the number of points within the plume was generally limited to mostly 3–5 despite such a configuration. To overcome this limitation and to take advantage of the wind variability, the inversion considers, at each location, the binning of the measurements over successive windows of equal time lengths or over sectors of wind direction. The results obtained when binning the data over sectors of wind direction appear to be more precise than those obtained when binning over time windows of equal durations, with an average relative error of approximately 23% in the emission rate estimates and an average error of 7.8 m for the location estimates, for the 26 controlled releases analyzed in this study.

The inversion framework by Kumar *et al.* (2021), initially tested with the very brief controlled releases of the TADI-2018 campaign, is used to process the mobile measurements during the much longer releases analyzed here. The corresponding inversions provide more precise estimates of the release rates than those presented in Kumar *et al.* (2021) since the method can rely on the analysis of a larger number of plume cross-sections. These estimates are also slightly more precise than the release rate estimates provided by the inversions based on the stationary measurements, with an average relative error of approximately 20%. However, the errors in the estimates of the release locations are much larger when using the mobile measurements with an average location error of approximately 29 m.

The increase of the length of the releases associated with longer measurement time-series tend to support an improvement of the results but such an improvement is limited by the impact of model biases, especially for the localization of the releases. While this impact is highlighted by the analysis, the model biases themselves are difficult to characterize. The precision of the release rate estimates slightly degrades when fixing the location of the sources to its actual position in the inversion frameworks. The inversion frameworks lack the ability to derive or to limit the impact of the effective injection height of the releases, especially since the vertical diffusion of the model is difficult to adjust. However, overall, all approaches provide good estimates of the release rates, and, when using the fixed-point data, of the release locations.

ACKNOWLEDGEMENTS

This work was supported by the Chaire Industrielle Trace ANR-17-CHIN-0004-01 co-funded by the ANR French national research agency, TotalEnergies-Raffinage Chimie, SUEZ, and THALES ALENIA SPACE.

AUTHOR CONTRIBUTIONS

Pramod Kumar: Conceptualization; data curation; formal analysis; investigation; methodology; software; validation; visualization; writing – original draft; writing – review and editing. **Grégoire Broquet:** Conceptualization; formal analysis; funding acquisition; investigation; methodology; project administration; supervision; validation; visualization; writing – original draft; writing – review and editing. **Christopher Caldow:** Conceptualization; data curation; investigation; methodology; project administration; validation; visualization; writing – original draft; writing – review and editing. **Olivier Laurent:** Conceptualization; data curation; funding acquisition; investigation; methodology; project administration; supervision; validation; writing – review and editing. **Susan Gichuki:** Conceptualization; data curation; investigation; writing – review and editing. **Ford Cropley:** Conceptualization; data curation; investigation; writing – review and editing. **Camille Yver-Kwok:** Conceptualization; data curation; funding acquisition; investigation; writing – review and editing. **Bonaventure Fontanier:** Conceptualization; formal analysis; investigation; writing – review and editing. **Thomas Lauvaux:** Conceptualization; investigation; writing – review and editing. **Michel Ramonet:** Conceptualization; funding acquisition; resources; writing – review and editing. **Adil Shah:** Conceptualization; data curation; project administration; writing – review and editing. **Guillaume Berthe:** Conceptualization; data curation; investigation; resources; validation; writing – review and editing. **Frédéric Martin:** Conceptualization; data curation; investigation; resources; validation; writing – review and editing. **Olivier Duclaux:** Conceptualization; data curation; resources; validation; writing – review and editing. **Catherine Juery:** Conceptualization; data curation; funding acquisition; project administration; resources; supervision; validation; writing – review and editing. **Caroline Bouchet:** Conceptualization; funding acquisition; writing – review and editing. **Joseph Pitt:** Conceptualization; formal analysis; writing – review and editing. **Philippe Ciais:** Conceptualization; funding acquisition; project administration; resources; supervision; writing – review and editing.

DATA AVAILABILITY STATEMENT

The dataset was collected and the codes developed in the frame of the Chaire Indutrielle Trace ANR-17-CHIN-0004-01. They are accessible upon request to the corresponding author.

ORCID

Pramod Kumar https://orcid.org/0000-0003-4528-1515
Grégoire Broquet https://orcid.org/0000-0001-7447-6907
Adil Shah https://orcid.org/0000-0002-5692-3715

REFERENCES

Albertson, J.D., Harvey, T., Foderaro, G., Zhu, P., Zhou, X., Ferrari, S., Amin, M.S., Modrak, M., Brantley, H. and Thoma, E.D. (2016) A Mobile sensing approach for regional surveillance of fugitive methane emissions in oil and gas production. *Environmental Science & Technology*, 50(5), 2487–2497. https://doi.org/10.1021/acs.est.5b05059.

Alvarez, R.A., Zavala-Araiza, D., Lyon, D.R., Allen, D.T., Barkley, Z.R., Brandt, A.R., Davis, K.J., Herndon, S.C., Jacob, D.J., Karion, A., Kort, E.A., Lamb, B.K., Lauvaux, T., Maasakkers, J.D., Marchese, A.J., Omara, M., Pacala, S.W., Peischl, J., Robinson, A.L. and Hamburg, S.P. (2018) Assessment of methane emissions from the U.S. oil and gas supply chain. *Science (New York, N.Y.)*, 361(6398), 186–188. https://doi.org/10.1126/science.aar7204.

Ars, S., Broquet, G., Yver Kwok, C., Roustan, Y., Wu, L., Arzoumanian, E. and Bousquet, P. (2017) Statistical atmospheric inversion of local gas emissions by coupling the tracer release technique and local-scale transport modelling: a test case with controlled methane emissions. *Atmospheric Measurement Techniques*, 10(12), 5017–5037. https://doi.org/10.5194/amt-10-5017-2017.

Ben Salem, N. (2014) Modélisation directe et inverse de la dispersion atmosphérique en milieux complexes. http://air.ec-lyon.fr/Doc/Theses/Thesis-BenSalem-N-2014.pdf.

Bergamaschi, P., Karstens, U., Manning, A.J., Saunois, M., Tsuruta, A., Berchet, A., Vermeulen, A.T., Arnold, T., Janssens-Maenhout, G., Hammer, S., Levin, I., Schmidt, M., Ramonet, M., Lopez, M., Lavric, J., Aalto, T., Chen, H., Feist, D.G., Gerbig, C. and Dlugokencky, E. (2018) Inverse modelling of European CH₄ emissions during 2006–2012 using different inverse models and reassessed atmospheric observations. *Atmospheric Chemistry and Physics*, 18(2), 901–920. https://doi.org/10.5194/acp-18-901-2018.

Bocquet, M. (2005) Reconstruction of an atmospheric tracer source using the principle of maximum entropy. I: theory. *Quarterly Journal of the Royal Meteorological Society.*, 131, 2209–2223. https://doi.org/10.1256/qj.04.68.

Brantley, H.L., Thoma, E.D., Squier, W.C., Guven, B.B. and Lyon, D. (2014) Assessment of methane emissions from oil and gas production pads using Mobile measurements. *Environmental Science & Technology*, 48(24), 14508–14515. https://doi.org/10.1021/es503070q.

Briggs, G.A. (1975) Plume rise predictions. Lectures on air pollution and environment impact analyses. *American Meteorological Society*, 10, 59–111.

Carruthers, D.J., Weng, W.S., Hunt, J.R.C., Holroyd, R.J., McHugh, C.A. and Dyster, S.. (2020) Plume/puff spread and mean concentration module specifications. Technical Report ADMS 5.2, P10/01Y/17, P12/01Y/17. https://www.cerc.co.uk/environmental-software/assets/data/doc_techspec/P10_01.P12_01.pdf.

Caulton, D.R., Li, Q., Bou-Zeid, E., Fitts, J.P., Golston, L.M., Pan, D., Lu, J., Lane, H.M., Buchholz, B., Guo, X., McSpiritt, J., Wendt, L. and Zondlo, M.A. (2018) Quantifying uncertainties from mobile-laboratory-derived emissions of well pads using inverse Gaussian methods. *Atmospheric Chemistry and*

Physics, 18(20), 15145–15168. https://doi.org/10.5194/acp-18-15145-2018.

de Gouw, J.A., Veefkind, J.P., Roosenbrand, E., Dix, B., Lin, J.C., Landgraf, J. and Levelt, P.F. (2020) Daily satellite observations of methane from oil and gas production regions in the United States. *Scientific Reports*, 10(1), 1379. https://doi.org/10.1038/s41598-020-57678-4.

Draxler, R.R. (1976) Determination of atmospheric diffusion parameters. *Atmospheric Environment (1967)*, 10(2), 99–105. https://doi.org/10.1016/0004-6981(76)90226-2.

Dyer, A.J. (1974) A review of flux-profile relationships. *Boundary-Layer Meteorology*, 7(3), 363–372. https://doi.org/10.1007/BF00240838.

Edie, R., Robertson, A.M., Field, R.A., Soltis, J., Snare, D.A., Zimmerle, D., Bell, C.S., Vaughn, T.L. and Murphy, S.M. (2020) Constraining the accuracy of flux estimates using OTM 33A. *Atmospheric Measurement Techniques*, 13(1), 341–353. https://doi.org/10.5194/amt-13-341-2020.

Feitz, A., Schroder, I., Phillips, F., Coates, T., Negandhi, K., Day, S., Luhar, A., Bhatia, S., Edwards, G., Hrabar, S., Hernandez, E., Wood, B., Naylor, T., Kennedy, M., Hamilton, M., Hatch, M., Malos, J., Kochanek, M., Reid, P. and Griffith, D. (2018) The Ginninderra CH4 and CO2 release experiment: an evaluation of gas detection and quantification techniques. *International Journal of Greenhouse Gas Control*, 70, 202–224. https://doi.org/10.1016/j.ijggc.2017.11.018.

Foster-Wittig, T.A., Thoma, E.D. and Albertson, J.D. (2015) Estimation of point source fugitive emission rates from a single sensor time series: a conditionally-sampled Gaussian plume reconstruction. *Atmospheric Environment*, 115, 101–109. https://doi.org/10.1016/j.atmosenv.2015.05.042.

Fox, T.A., Barchyn, T.E., Risk, D., Ravikumar, A.P. and Hugenholtz, C.H. (2019) A review of close-range and screening technologies for mitigating fugitive methane emissions in upstream oil and gas. *Environmental Research Letters*, 14(5), 053002. https://doi.org/10.1088/1748-9326/ab0cc3.

FprEN-17628. (2021) Fugitive and diffuse emissions of common concern to industry sectors- Standard method to determine diffuse emissions of volatile organic compounds into the atmosphere, CEN/TC 264/WG 38 N 133. CEN/TC 264/WG 38 N 133.

Frankenberg, C. (2005) Assessing methane emissions from global space-borne observations. *Science*, 308(5724), 1010–1014. https://doi.org/10.1126/science.1106644.

Gryning, S.E., Holtslag, A.A.M., Irwin, J.S. and Sivertsen, B. (1987) Applied dispersion modelling based on meteorological scaling parameters. *Atmospheric Environment (1967)*, 21(1), 79–89. https://doi.org/10.1016/0004-6981(87)90273-3.

Hanna, S.R., Briggs, G.A. and Hosker, R.P.J. (1982) *Handbook on Atmospheric Diffusion*. United States: Technical Information Center, U. S. Department of Energy. https://doi.org/10.2172/5591108.

Hoinaski, L., Franco, D. and de Melo Lisboa, H. (2016) Comparison of plume lateral dispersion coefficients schemes: effect of averaging time. *Atmospheric Pollution Research*, 7(1), 134–141. https://doi.org/10.1016/j.apr.2015.08.004.

Hu, H., Landgraf, J., Detmers, R., Borsdorff, T., Aan de Brugh, J., Aben, I., Butz, A. and Hasekamp, O. (2018) Toward global mapping of methane with TROPOMI: first results and Intersatellite comparison to GOSAT. *Geophysical Research Letters.*, 45, 3682–3689. https://doi.org/10.1002/2018GL077259.

IPCC. (2013) Climate change 2013 - the physical science basis. In: Stocker, T.F., Qin, D., Plattner, G.K., Tignor, M.M.B., Allen, S.K., Boschung, J., Nauels, A., Xia, Y., Bex, V. and Midgley, P.M. (Eds.) *Climate Change 2013 the Physical Science Basis: Working Group I Contribution to the Fifth Assessment Report of the Intergovernmental Panel on Climate Change*. United Kingdom and New York, NY, USA: Cambridge University Press, 1535 pp. https://doi.org/10.1017/CBO9781107415324.

Jacob, D.J., Turner, A.J., Maasakkers, J.D., Sheng, J., Sun, K., Liu, X., Chance, K., Aben, I., McKeever, J. and Frankenberg, C. (2016) Satellite observations of atmospheric methane and their value for quantifying methane emissions. *Atmospheric Chemistry and Physics*, 16(22), 14371–14396. https://doi.org/10.5194/acp-16-14371-2016.

Keats, A., Yee, E. and Lien, F.-S. (2007) Bayesian inference for source determination with applications to a complex urban environment. *Atmospheric Environment*, 41(3), 465–479. https://doi.org/10.1016/j.atmosenv.2006.08.044.

Kumar, P., Broquet, G., Yver-Kwok, C., Laurent, O., Gichuki, S., Caldow, C., Cropley, F., Lauvaux, T., Ramonet, M., Berthe, G., Martin, F., Duclaux, O., Juery, C., Bouchet, C. and Ciais, P. (2021) Mobile atmospheric measurements and local-scale inverse estimation of the location and rates of brief CH4 and CO2 releases from point sources. *Atmospheric Measurement Techniques*, 14(9), 5987–6003. https://doi.org/10.5194/amt-14-5987-2021.

Kumar, P., Feiz, A.A., Singh, S.K., Ngae, P. and Turbelin, G. (2015) Reconstruction of an atmospheric tracer source in an urban-like environment. *Journal of Geophysical Research*, 120(24), 12589–12604. https://doi.org/10.1002/2015JD024110.

Loh, Z., Leuning, R., Zegelin, S., Etheridge, D., Bai, M., Naylor, T. and Griffith, D. (2009) Testing Lagrangian atmospheric dispersion modelling to monitor CO2 and CH4 leakage from geosequestration. *Atmospheric Environment*, 43(16), 2602–2611. https://doi.org/10.1016/j.atmosenv.2009.01.053.

Luhar, A.K., Etheridge, D.M., Leuning, R., Loh, Z.M., Jenkins, C.R. and Yee, E. (2014) Locating and quantifying greenhouse gas emissions at a geological CO2 storage site using atmospheric modeling and measurements. *Journal of Geophysical Research: Atmospheres*, 119(18), 10959–10979. https://doi.org/10.1002/2014JD021880.

Marchuk, G.I. (1995) Adjoint equations and analysis of complex systems. In: *Adjoint Equations and Analysis of Complex Systems*. Netherlands: Springer. https://doi.org/10.1007/978-94-017-0621-6.

Mønster, J., Kjeldsen, P. and Scheutz, C. (2019) Methodologies for measuring fugitive methane emissions from landfills – a review. *In Waste Management.*, 87, 835–859. https://doi.org/10.1016/j.wasman.2018.12.047.

Nisbet, E.G., Dlugokencky, E.J. and Bousquet, P. (2014) Atmospheric science. Methane on the rise--again. *Science (New York, N.Y.)*, 343(6170), 493–495. https://doi.org/10.1126/science.1247828.

Pison, I., Berchet, A., Saunois, M., Bousquet, P., Broquet, G., Conil, S., Delmotte, M., Ganesan, A., Laurent, O., Martin, D., O'Doherty, S., Ramonet, M., Spain, T.G., Vermeulen, A. and Yver Kwok, C. (2018) How a European network may help with estimating methane emissions on the French national scale.

Atmospheric Chemistry and Physics, 18(5), 3779–3798. https://doi.org/10.5194/acp-18-3779-2018.

Pudykiewicz, J.A. (1998) Application of adjoint tracer transport equations for evaluating source parameters. *Atmospheric Environment*, 32(17), 3039–3050. https://doi.org/10.1016/S1352-2310(97)00480-9.

Qian, W. and Venkatram, A. (2011) Performance of steady-state dispersion models under low wind-speed conditions. *Boundary-Layer Meteorology*, 138(3), 475–491. https://doi.org/10.1007/s10546-010-9565-1.

Ravikumar, A.P., Sreedhara, S., Wang, J., Englander, J., Roda-Stuart, D., Bell, C., Zimmerle, D., Lyon, D., Mogstad, I., Ratner, B. and Brandt, A.R. (2019) Single-blind inter-comparison of methane detection technologies – results from the Stanford/EDF Mobile monitoring challenge. *Elementa: Science of the Anthropocene*, 7(1), 37. https://doi.org/10.1525/elementa.373.

Riddick, S.N., Connors, S., Robinson, A.D., Manning, A.J., Jones, P.S.D., Lowry, D., Nisbet, E., Skelton, R.L., Allen, G., Pitt, J. and Harris, N.R.P. (2017) Estimating the size of a methane emission point source at different scales: from local to landscape. *Atmospheric Chemistry and Physics*, 17(12), 7839–7851. https://doi.org/10.5194/acp-17-7839-2017.

Saunois, M., Stavert, A.R., Poulter, B., Bousquet, P., Canadell, J.G., Jackson, R.B., Raymond, P.A., Dlugokencky, E.J., Houweling, S., Patra, P.K., Ciais, P., Arora, V.K., Bastviken, D., Bergamaschi, P., Blake, D.R., Brailsford, G., Bruhwiler, L., Carlson, K.M., Carrol, M. and Zhuang, Q. (2020) The global methane budget 2000–2017. *Earth System Science Data*, 12(3), 1561–1623. https://doi.org/10.5194/essd-12-1561-2020.

Shah, A., Pitt, J.R., Ricketts, H., Leen, J.B., Williams, P.I., Kabbabe, K., Gallagher, M.W. and Allen, G. (2020) Testing the near-field Gaussian plume inversion flux quantification technique using unmanned aerial vehicle sampling. *Atmospheric Measurement Techniques*, 13(3), 1467–1484. https://doi.org/10.5194/amt-13-1467-2020.

Sharan, M., Issartel, J.-P.P., Singh, S.K. and Kumar, P. (2009) An inversion technique for the retrieval of single-point emissions from atmospheric concentration measurements. *Proceedings of the Royal Society A: Mathematical, Physical and Engineering Sciences*, 465(2107), 2069–2088. https://doi.org/10.1098/rspa.2008.0402.

Sharan, M. and Kumar, P. (2009) An analytical model for crosswind integrated concentrations released from a continuous source in a finite atmospheric boundary layer. *Atmospheric Environment*, 43(14), 2268–2277. https://doi.org/10.1016/j.atmosenv.2009.01.035.

Sharan, M., Singh, S.K. and Issartel, J.P. (2012) Least square data assimilation for identification of the point source emissions. *Pure and Applied Geophysics.*, 169, 483–497. https://doi.org/10.1007/s00024-011-0382-3.

Thomson, D.J. and Manning, A.J. (2001) Along-wind dispersion In light wind conditions. *Boundary-Layer Meteorology*, 98(2), 341–358. https://doi.org/10.1023/A:1026542924429.

Varon, D.J., Jacob, D.J., McKeever, J., Jervis, D., Durak, B.O.A., Xia, Y. and Huang, Y. (2018) Quantifying methane point sources from fine-scale satellite observations of atmospheric methane plumes. *Atmospheric Measurement Techniques*, 11(10), 5673–5686. https://doi.org/10.5194/amt-11-5673-2018.

von Fischer, J.C., Cooley, D., Chamberlain, S., Gaylord, A., Griebenow, C.J., Hamburg, S.P., Salo, J., Schumacher, R., Theobald, D. and Ham, J. (2017) Rapid, vehicle-based identification of location and magnitude of urban natural gas pipeline leaks. *Environmental Science & Technology*, 51(7), 4091–4099. https://doi.org/10.1021/acs.est.6b06095.

Zavala-Araiza, D., Allen, D.T., Harrison, M., George, F.C. and Jersey, G.R. (2015) Allocating methane emissions to natural gas and oil production from shale formations. *ACS Sustainable Chemistry & Engineering*, 3(3), 492–498. https://doi.org/10.1021/sc500730x.

Zhang, Y., Gautam, R., Pandey, S., Omara, M., Maasakkers, J.D., Sadavarte, P., Lyon, D., Nesser, H., Sulprizio, M.P., Varon, D.J., Zhang, R., Houweling, S., Zavala-Araiza, D., Alvarez, R.A., Lorente, A., Hamburg, S.P., Aben, I. and Jacob, D.J. (2020) Quantifying methane emissions from the largest oil-producing basin in the United States from space. *Science Advances.*, 6, eaaz5120. https://doi.org/10.1126/sciadv.aaz5120.

Zhou, X., Montazeri, A. and Albertson, J.D. (2019) Mobile sensing of point-source gas emissions using Bayesian inference: an empirical examination of the likelihood function. *Atmospheric Environment*, 218, 116981. https://doi.org/10.1016/j.atmosenv.2019.116981.

SUPPORTING INFORMATION

Additional supporting information may be found online in the Supporting Information section at the end of this article.

How to cite this article: Kumar, P., Broquet, G., Caldow, C., Laurent, O., Gichuki, S., Cropley, F. *et al.* (2022) Near-field atmospheric inversions for the localization and quantification of controlled methane releases using stationary and mobile measurements. *Quarterly Journal of the Royal Meteorological Society*, 1–27. Available from: https://doi.org/10.1002/qj.4283

APPENDIX A

Derivation of optimal release rates for a given release location when using the mobile measurements

In the frame of the inversion when using mobile measurements, the Gaussian model (Equation 1), provides a linear relationship between the mole fraction at a given location and the release rate q for a fixed release location $\mathbf{x}^{\text{horiz}}$. Thus, the modelled amplitude A_{mi} of a plume cross-section can be computed as:

$$A_{mi} = q\, R_{mi} \tag{A1}$$

where R_{mi} is the amplitude simulated with the Gaussian model using a unity emission rate (A_{mi} and R_{mi} depending on $\mathbf{x}^{\text{horiz}}$). Accordingly, the cost function J^{mob} (Equation 9)

can be rewritten as:

$$J^{\text{mob}}\left(\mathbf{x}^{\text{horiz}}, q\right) = \sum_{i=1}^{N_{\text{p}}} \left[\frac{A_{oi} - q\, R_{mi}}{A_{oi}}\right]^2 + J_{\text{w}} \tag{A2}$$

where J_{w} (Equation 11) is independent of the release rate q. When fixing $\mathbf{x}^{\text{horiz}}$, the minimum of the quadratic function $J^{\text{mob}}_{\mathbf{x}^{\text{horiz}}}(q) = J^{\text{mob}}\left(\mathbf{x}^{\text{horiz}}, q\right)$ (Equation A2) can be found by solving for $\frac{\partial J^{\text{mob}}_{\mathbf{x}^{\text{horiz}}}}{\partial q} = 0$, that is,

$$q^{\text{opt}}_{\mathbf{x}^{\text{horiz}}} = \frac{\sum_{i=1}^{N_{\text{p}}} \left(\frac{R_{mi}}{A_{oi}}\right)}{\sum_{i=1}^{N_{\text{p}}} \left(\frac{R_{mi}}{A_{oi}}\right)^2} \tag{A3}$$